

NASA Technical Memorandum 4786

Extraction of Lateral-Directional Stability and Control Derivatives for the Basic F-18 Aircraft at High Angles of Attack

Kenneth W. Iliff and Kon-Sheng Charles Wang

February 1997



Extraction of Lateral-Directional Stability and Control Derivatives for the Basic F-18 Aircraft at High Angles of Attack

Kenneth W. Iliff
*Dryden Flight Research Center
Edwards, California*

Kon-Sheng Charles Wang
*SPARTA, Inc.
Lancaster, California*



National Aeronautics and
Space Administration

Office of Management

Scientific and Technical
Information Program

1997

CONTENTS

	<u>Page</u>
ABSTRACT	1
NOMENCLATURE	1
INTRODUCTION.....	3
VEHICLE DESCRIPTION.....	4
INSTRUMENTATION AND DATA ACQUISITION	5
PARAMETER IDENTIFICATION METHODOLOGY	6
RESULTS AND DISCUSSION	9
Parameter Identification Maneuvers	9
Extracted Stability and Control Derivatives	11
CONCLUDING REMARKS	12
REFERENCES	14

TABLE

F-18 aerodynamic control surface position and rate limits.....	5
--	---

FIGURES

1. NASA F-18 High Angle-of-Attack Research Vehicle.....	16
2. Three-view of the F-18 with major dimensions shown	17
3. Maximum likelihood estimation concept with state and measurement noise.....	18
4. Time-history data from a typical lateral-directional PID maneuver at low AOA	19
5. Differential control surface deflection schedule due to aileron input (with ARI).....	23
6. Differential control surface deflection schedule due to rudder input (with RAI).....	23
7. Time-history data from a typical lateral-directional PID maneuver at high AOA	24
8. Sideslip derivatives as functions of AOA	29
9. Equivalent lateral control derivatives as functions of AOA	30
10. Rudder derivatives as functions of AOA.....	32
11. Rotary derivations as functions of AOA	33

ABSTRACT

The results of parameter identification to determine the lateral-directional stability and control derivatives of an F-18 research aircraft in its basic hardware and software configuration are presented. The derivatives are estimated from dynamic flight data using a specialized identification program developed at NASA Dryden Flight Research Center. The formulation uses the linearized aircraft equations of motions in their continuous/discrete form and a maximum likelihood estimator that accounts for both state and measurement noise. State noise is used to model the uncommanded forcing function caused by unsteady aerodynamics, such as separated and vortical flows, over the aircraft. The derivatives are plotted as functions of angle of attack between 3° and 47° and compared with wind-tunnel predictions. The quality of the derivative estimates obtained by parameter identification is somewhat degraded because the maneuvers were flown with the aircraft's control augmentation system engaged, which introduced relatively high correlations between the control variables and response variables as a result of control motions from the feedback control system.

NOMENCLATURE

Abbreviations and Acronyms

AOA	angle of attack, deg
ARI	aileron-to-rudder interconnect
DFRC	NASA Dryden Flight Research Center, Edwards, California
FADS	flush airdata system
FCS	flight control system
HARV	High Angle-of-Attack Research Vehicle
HATP	High Angle-of-Attack Technology Program
LEF	leading-edge flap
LEX	leading-edge extension (wing-body strake)
NACA	National Advisory Committee for Aeronautics
PCM	pulse code modulation
PID	parameter identification
PROM	Programmable Read-Only Memory
RAI	rudder-to-aileron interconnect
TEF	trailing-edge flap

Symbols

a_Y	lateral acceleration, g
$\mathbf{A}, \mathbf{B}, \mathbf{C}, \mathbf{D}, \mathbf{F}, \mathbf{G}$	system matrices
C_{l_p}	coefficient of rolling moment due to roll rate, rad^{-1}
C_{l_r}	coefficient of rolling moment due to yaw rate, rad^{-1}

$C_{l_{\beta}}$	coefficient of rolling moment due to sideslip, deg^{-1}
$C_{l_{\delta_a}}$	coefficient of rolling moment due to aileron deflection, deg^{-1}
$C_{l_{\delta_{dh}}}$	coefficient of rolling moment due to differential horizontal stabilator deflection, deg^{-1}
$C_{l_{\delta_L}}$	coefficient of rolling moment due to lateral deflection, deg^{-1}
$C_{l_{\delta_r}}$	coefficient of rolling moment due to rudder deflection, deg^{-1}
C_{n_p}	coefficient of yawing moment due to roll rate, rad^{-1}
C_{n_r}	coefficient of yawing moment due to yaw rate, rad^{-1}
$C_{n_{\beta}}$	coefficient of yawing moment due to sideslip, deg^{-1}
$C_{n_{\delta_a}}$	coefficient of yawing moment due to aileron deflection, deg^{-1}
$C_{n_{\delta_{dh}}}$	coefficient of yawing moment due to differential horizontal stabilator deflection, deg^{-1}
$C_{n_{\delta_L}}$	coefficient of yawing moment due to lateral deflection, deg^{-1}
$C_{n_{\delta_r}}$	coefficient of yawing moment due to rudder deflection, deg^{-1}
$C_{Y_{\beta}}$	coefficient of lateral force due to sideslip, deg^{-1}
$C_{Y_{\delta_a}}$	coefficient of lateral force due to aileron deflection, deg^{-1}
$C_{Y_{\delta_{dh}}}$	coefficient of lateral force due to differential horizontal stabilator deflection, deg^{-1}
$C_{Y_{\delta_L}}$	coefficient of lateral force due to lateral deflection, deg^{-1}
$C_{Y_{\delta_r}}$	coefficient of lateral force due to rudder deflection, deg^{-1}
f	system state function
g	system observation function
\mathbf{GG}^*	measurement noise covariance matrix
\mathbf{H}	approximation to the information matrix
J	cost function
N	number of time points
\mathbf{n}	state noise vector
p	roll rate, deg/sec
\mathbf{R}	innovation covariance matrix
r	yaw rate, deg/sec
t	time, sec
\mathbf{u}	known control input vector
\mathbf{x}	state vector
$\dot{\mathbf{x}}$	time derivative of state vector

$\tilde{\mathbf{x}}_{\xi}$	predicted state estimate
\mathbf{z}	observation vector
$\tilde{\mathbf{z}}_{\xi}$	predicted Kalman filter estimate
α	angle of attack, deg
β	angle of sideslip, deg
δ_a	aileron deflection, deg
δ_{a_p}	pilot aileron input, arc-in
δ_{dh}	differential horizontal stabilator deflection, deg
δ_L	equivalent combined lateral deflection of aileron and stabilator, deg
δ_{LEF}	leading-edge flap deflection, deg
δ_r	rudder deflection, deg
δ_{r_p}	pilot rudder input, in
δ_{TEF}	trailing-edge flap deflection, deg
η	measurement noise vector
ξ	unknown parameter vector
$\hat{\xi}$	estimate of ξ
∇_{ξ}	gradient with respect to ξ

Subscripts

i	general index
-----	---------------

INTRODUCTION

The NASA High-Angle-of-Attack Technology Program (HATP) was established in the mid-1980s to develop and validate some of the key technologies required for safe, predictable, and usable high-angle-of-attack (AOA) flight. The two prime objectives of the HATP were (1) to provide a flight-validated design methodology through experimental and computational methods that simulate and predict high-AOA aerodynamics, flight dynamics, and flying qualities; and (2) to improve aircraft agility at high AOA while expanding the usable high-AOA envelope. The HATP used a close integration of ground-based and flight activity, including wind-tunnel experiments, computational fluid dynamics models, piloted simulations, and flight tests to focus on three key areas: high-AOA aerodynamics, advanced high-AOA control concepts, and maneuver management (ref. 1).

To provide the critical flight validation element, an F-18 aircraft was loaned to NASA by the U.S. Navy. Extensive instrumentation was subsequently added for flight research purposes. The airplane was named the High-Angle-of-Attack Research Vehicle (HARV) (fig. 1). Access to full-scale flight conditions was deemed essential to address inherent shortcomings of subscale ground-testing techniques and to provide the confidence afforded through flight validation of new analytical methods and design concepts. Research flight testing was performed in three phases beginning in 1987 at NASA Dryden Flight Research Center (DFRC), Edwards, California. Flight testing was completed by the spring of 1996, meeting the three-phase program schedule of the HATP.

In phase I, which began in mid-1987 and continued through 1989, the HARV flew 101 research missions, investigating high-AOA flight up to 55°. Phase I examined developmental issues of the HARV research instrumentation suite and established initial aerodynamic correlations between predictions and in-flight measurements (e.g., of tail buffet and vortex burst location for the wing-body-strake vortices). Phase II involved major hardware and software modifications to the HARV, incorporating a multi-axis thrust-vectoring control system and research flight control system (FCS). This phase, from mid-1991 to late 1994, aggressively expanded the HARV flight envelope. Demonstrated capabilities include stabilized flight at 70° AOA and rolling at high rates at 65° AOA. Phase III flights began in 1995 and were completed by May 1996. These tests focused on the implementation of actuated forebody strakes mounted on the nose of the HARV to enhance directional control at high AOA.

A continuing objective of the flight program was the study of the stability and control characteristics of the F-18 aircraft during low-speed, high-AOA flight (refs. 2 and 3). This paper addresses the analysis and results of parameter identification (PID) conducted at DFRC to extract lateral-directional stability and control derivatives of the basic F-18 configuration from dynamic flight data. The results, based on 42 maneuvers from phase I flights 11 through 38 (flown between June 1987 and March 1988), were used to initially assess stability and control derivatives obtained from wind-tunnel tests and early flight test by the manufacturer and U.S. Navy. The derivatives were extracted using a DFRC-developed computer program, which uses the linearized aircraft equations of motion and a maximum likelihood estimator that accounts for state and measurement noise. The maneuvers analyzed ranged from 3° to 47° AOA. In this paper, the derivatives are estimated, plotted, and discussed relative to wind-tunnel predictions and flight maneuver quality.

VEHICLE DESCRIPTION

The aircraft testbed was the sixth full-scale developmental F-18 (fig. 1), a single place, twin-engine, fighter-attack aircraft built by McDonnell Douglas Corp. (St. Louis, Missouri) and Northrop Grumman Corp. (Los Angeles, California) for the U.S. Navy. The Navy previously used this particular aircraft (serial number 160780) for high-AOA and spin testing. The aircraft is powered by two General Electric (Lynn, Massachusetts) F404-GE-400 afterburning engines, each rated at approximately 16,000 lb static thrust at sea level. The F-18 features a midwing configuration with a wing-root leading-edge extension (LEX) that extends from the forward portion of the fuselage and blends into the wing. The configuration under study, (dating from 1987 to 1988) did not carry the LEX fence modification, introduced in late 1988, nor any of the thrust-vectoring enhancements used during phases II and III of the HATP flight program. The F-18 as flown carried no external stores and was highly instrumented for research purposes. The wingtip missile launch rails and missiles were replaced with specially designed airdata sensors and camera pods (explained later in the “Instrumentation and Data Acquisition” section). The in-flight refueling capability and tail-arresting hook were retained. Figure 2 shows a three-view drawing of the F-18, along with major physical characteristics.

The F-18 has five pairs of aerodynamic control surfaces: stabilators, rudders, ailerons, leading-edge flaps (LEFs), and trailing-edge flaps (TEFs). The twin vertical stabilizers, with trailing-edge rudders, are canted outboard at approximately 20° from the vertical. Pitch control is provided by the collective operation of the all-movable horizontal stabilators and the symmetric LEFs and TEFs. For flight above 25° AOA, symmetric LEFs are fixed to 33° full down. Though symmetric TEFs are scheduled with AOA below 25°, they are fixed to 0° deflection above 25° AOA. Roll control uses deflections of the ailerons (δ_a), differential horizontal stabilators (δ_{dh}), and asymmetric LEFs (δ_{LEF}) and TEFs (δ_{TEF}). Directional control is provided by symmetric rudder deflection (δ_r) and a rudder-to-aileron interconnect (RAI) between δ_r and both δ_a and δ_{dh} . In addition, the FCS augments lateral-directional control with an aileron-to-rudder interconnect (ARI), to be discussed with the RAI in the “Results and Discussion” section. Symmetric aileron droop and rudder toe-in are employed in the power approach configuration. A speed brake is on the upper aft fuselage, between the vertical stabilizers. The table provides maximum control surface positions and rate limits.

The computer-based FCS features digital inputs from redundant production sensor sets and airdata. The pilot commands provide automatic mode logic, gain scheduling, input-output management, and surface management. The FCS is a digitally-mechanized fly-by-wire control augmentation system. The standard F-18 version V8.3.3 flight control law is implemented on four 701B (General Electric, Lynn, Massachusetts) digital flight control computers, along with surface actuators and analog sensors, to provide a dual-failure operational capability. The FCS was developed with complete failure detection, failure management, and appropriate mode switching in the event of certain failures. A digital direct electrical control mode provides a fly-by-wire open-loop control law in case certain motion sensors fail. In addition, a mechanical control mode is provided in case the fly-by-wire control systems fail. This system provides a direct mechanical link from the pilot's stick to the longitudinal trim and stabilator actuators. The mechanical mode provides pitch and roll control from the pilot's stick to the stabilators.

F-18 aerodynamic control surface position and rate limits.		
Surface	Position limit, deg	Rate limit, deg/sec
Stabilator:		
Trailing-edge up	24	40
Trailing-edge down	10.5	40
Aileron:		
Trailing-edge up	24	100
Trailing-edge down	45	100
Rudder:		
Trailing-edge left	30	82
Trailing-edge right	30	82
TEF:		
Up	8	18
Down	45	18
LEF:		
Up	3	15
Down	33	15
Speed brake:		
Trailing-edge up	60	20 to 30

The mission computer provides MIL-STD-1553 multiplex bus control. This data bus provides an integrated control system and a standard interface for all equipment connected to the bus.

INSTRUMENTATION AND DATA ACQUISITION

Onboard data acquisition included standard parameters from the production F-18 MIL-STD-1553 data bus and from specialized research instrumentation such as accelerometers, rate gyros, control surface position transducers, and airdata sensors. Early in phase I, which included the flights studied here, airdata measurement was investigated with several techniques. Up to flight 16, a standard NACA noseboom-mounted probe was used for airdata. From flights 17 to 31, noseboom airdata were complemented with airdata from a right-wingtip-mounted NACA probe with

AOA and sideslip vanes. (Although the right wingtip probe was installed on flight 4, an acceptable calibration was not available until flight 17.) From flight 32 on, a swiveling (self-aligning) pitot probe with conventional AOA and sideslip vanes was mounted on the left wingtip (ref. 4). After flight 38, the noseboom probe was removed because it affected the forebody flow and thus the high-AOA stability and control of the aircraft. Shortly thereafter, a flush airdata system (FADS) was installed in the tip of the nose cone (ref. 5). Given the several airdata systems—each with different calibrations, calculated functions, and function revisions implemented over a relatively short time span—an assessment of true airdata early in phase I proved somewhat complicated. However, sufficiently accurate airdata were obtained for the PID analysis presented here.

For purposes of in-flight aircraft flow visualization, the airplane was equipped with a smoker system (refs. 6 and 7) and a surface flow visualization system (refs. 8 and 9). Flow visualization and associated pressure data have been used to validate computational fluid dynamics models and wind-tunnel results. Video data were obtained with two forward-facing, black-and-white video cameras mounted on the inboard side of the vertical tails; a color video camera on the left wingtip pod; a still 35-mm camera on the right wingtip pod; and another color video camera behind the cockpit, on the turtleback, looking aft. Data measurements, including video signals from any two of the onboard video cameras, were sent by telemetry to the ground for real-time monitoring and recording.

The telemetry system consisted of two independent, asynchronous pulse code modulation (PCM) data encoders, each with a basic PCM word size of 10 bits. The output of the encoders was sent by telemetry to the ground; no onboard recording of the PCM data was provided in the airplane. Special provisions were incorporated in the data acquisition system for higher resolution signals of certain types of data. For example, data collected from rate gyros, linear accelerometers, and the inertial measuring system were encoded into 14-bit words. The 16-bit words from the MIL-STD-1553B bus were inserted in two 10-bit PCM words to obtain the parameters involving the digital FCS.

Flight data used in the present analysis were thinned to a final sample rate of 40 Hz from ground-recorded data received via telemetry from the aircraft. Airdata used in the present analysis were taken from either the noseboom or right wingtip boom, depending on the flight number as mentioned previously. Measurements of AOA and sideslip were corrected for center-of-gravity offset. Wind-vane data were also corrected for upwash, sidewash, and boom-bending effects. Linear accelerometer data were corrected for instrument offsets from the center of gravity in the PID program. Transducers were also available for measuring closed-loop and open-loop input variables, response variables, engine operation, and fuel consumption, from which instantaneous mass and inertia characteristics were calculated.

Furthermore, before the maneuvers were analyzed, the data were corrected for time lags introduced by sensor dynamics and signal filtering. Making these corrections is critical to adequately estimate the stability and control derivatives (ref. 10).

PARAMETER IDENTIFICATION METHODOLOGY

A primary purpose of the HARV flight program was to evaluate the aircraft configuration flying at high AOA. It is well known that while flying at high AOA where there is significant flow separation and vortical flow over the aircraft that the vehicle will exhibit uncommanded motions. Reference 11 presents a discussion of maneuver difficulties and related analysis issues under these conditions for the 3/8-scale F-15 Remotely Piloted Vehicle aircraft at AOA from -20° to 53° . At high AOA, the uncommanded motions vary from relatively small amplitude, high-frequency disturbances to very large wing rocking motions to complete roll-off from the flight condition. In addition to being bothersome to the pilot, the motions also complicate the extraction of stability and control derivatives from the planned stability and control maneuvers (ref. 11). The present analysis was also made difficult by the F-18 flight control system necessarily interconnecting certain control surfaces together, an important issue to be expanded upon

in the next section. To better analyze the existing maneuvers, it was necessary to account for the uncommanded portions of the aircraft motion.

The procedure implemented in this analysis uses state noise to model the uncommanded forcing function. References 12, 13, and 14 completely describe the technique. The technique applied to the F-18 data also required that the normal aircraft equations of motion be linear in the aerodynamic coefficients; this presented no particular difficulty because the normal stability and control derivatives were already locally linear approximations of nonlinear aircraft aerodynamics.

To perform the analysis presented here, an existing parameter estimation computer program was modified to properly account for the additional complexity required to include the effects of the state noise (commands due to separated and vortical flows) on the stability and control maneuvers. A brief description of the state noise algorithm follows.

It is possible to make a precise, mathematically probabilistic statement of the parameter estimation problem. The first step is to define the general system model (aircraft equations of motion). This model can be written in the continuous/discrete form as

$$\mathbf{x}(t_0) = \mathbf{x}_0 \quad (1)$$

$$\dot{\mathbf{x}}(t) = f[\mathbf{x}(t), \mathbf{u}(t), \xi] + \mathbf{F}(\xi)\mathbf{n}(t) \quad (2)$$

$$\mathbf{z}(t_i) = g[\mathbf{x}(t_i), \mathbf{u}(t_i), \xi] + \mathbf{G}(\xi)\eta_i \quad (3)$$

where \mathbf{x} is the state vector, \mathbf{z} is the observation vector, f and g are system state and observation functions, \mathbf{u} is the known control input vector, ξ is the unknown parameter vector, \mathbf{n} is the state noise vector, η is the measurement noise vector, \mathbf{F} and \mathbf{G} are system matrices, and t is time. The state noise vector \mathbf{n} is assumed to be zero-mean white Gaussian and stationary, and the measurement noise vector η is assumed to be a sequence of independent Gaussian random variables with zero-mean and identity covariance. For each possible estimate of the unknown parameters, a probability that the aircraft response time histories attain values near the observed values can then be defined. The maximum likelihood estimates are defined as those that maximize this probability. Maximum likelihood estimation has many desirable statistical characteristics; for example, it yields asymptotically unbiased, consistent, and efficient estimates.

If equations (2) and (3) are linearized (as is the case for the stability and control derivatives in the aircraft problem), then

$$\mathbf{x}(t_0) = \mathbf{x}_0 \quad (4)$$

$$\dot{\mathbf{x}}(t) = \mathbf{Ax}(t) + \mathbf{Bu}(t) + \mathbf{Fn}(t) \quad (5)$$

$$\mathbf{z}(t_i) = \mathbf{Cx}(t_i) + \mathbf{Du}(t_i) + \mathbf{G}\eta_i \quad (6)$$

where \mathbf{A} , \mathbf{B} , \mathbf{C} , and \mathbf{D} are system matrices.

When state noise is important, the nonlinear form of equations (1) through (3) is intractable. For the linear model defined by equations (4) through (6), the cost function that accounts for state noise is

$$J(\xi) = \frac{1}{2} \sum_{i=1}^N \left[\mathbf{z}(t_i) - \tilde{\mathbf{z}}_{\xi}(t_i) \right]^* \mathbf{R}^{-1} \left[\mathbf{z}(t_i) - \tilde{\mathbf{z}}_{\xi}(t_i) \right] + \frac{1}{2} N \ln |\mathbf{R}| \quad (7)$$

where \mathbf{R} is the innovation covariance matrix and N is the number of time points. The $\tilde{\mathbf{z}}_\xi(t_i)$ term is the Kalman-filtered estimate of \mathbf{z} . (The cost function is the function of the difference between the measured and computed time histories.)

To minimize the cost function $J(\xi)$, we can apply the Newton-Raphson algorithm, which chooses successive estimates of the vector of unknown coefficients $\hat{\xi}$. Let L be the iteration number. The $L + 1$ estimate of $\hat{\xi}$ is then obtained from the L estimate as follows:

$$\hat{\xi}_{L+1} = \hat{\xi}_L - \left[\nabla_\xi^2 J(\hat{\xi}_L) \right]^{-1} \left[\nabla_\xi^* J(\hat{\xi}_L) \right] \quad (8)$$

If \mathbf{R} is assumed fixed, the first and second gradients are defined as

$$\nabla_\xi J(\xi) = - \sum_{i=1}^N \left[\mathbf{z}(t_i) - \tilde{\mathbf{z}}_\xi(t_i) \right]^* (\mathbf{G}\mathbf{G}^*)^{-1} \left[\nabla_\xi \tilde{\mathbf{z}}_\xi(t_i) \right] \quad (9)$$

$$\begin{aligned} \nabla_\xi^2 J(\xi) = & \sum_{i=1}^N \left[\nabla_\xi \tilde{\mathbf{z}}_\xi(t_i) \right]^* (\mathbf{G}\mathbf{G}^*)^{-1} \left[\nabla_\xi \tilde{\mathbf{z}}_\xi(t_i) \right] \\ & - \sum_{i=1}^N \left[\mathbf{z}(t_i) - \tilde{\mathbf{z}}_\xi(t_i) \right]^* (\mathbf{G}\mathbf{G}^*)^{-1} \left[\nabla_\xi^2 \tilde{\mathbf{z}}_\xi(t_i) \right] \end{aligned} \quad (10)$$

The Gauss-Newton approximation to the second gradient is

$$\nabla_\xi^2 J(\xi) \equiv \sum_{i=1}^N \left[\nabla_\xi \tilde{\mathbf{z}}_\xi(t_i) \right]^* (\mathbf{G}\mathbf{G}^*)^{-1} \left[\nabla_\xi \tilde{\mathbf{z}}_\xi(t_i) \right] \quad (11)$$

The Gauss-Newton approximation, which in past reports by the first author was sometimes referred to as modified Newton-Raphson, is computationally much easier than the Newton-Raphson approximation because the second gradient of the innovation never needs to be calculated.

Figure 3 illustrates the maximum likelihood estimation concept. The measured response is compared with the estimated response, and the difference between these responses is called the response error. The cost function of equation (7) includes this response error. The minimization algorithm is used to find the coefficient values that minimize the cost function. Each iteration of this algorithm provides a new estimate of the unknown coefficients on the basis of the response error. These new estimates are then used to update values of the coefficients of the mathematical model, providing a new estimated response, and therefore, a new response error. Updating of the mathematical model continues iteratively until a convergence criterion is satisfied. The estimates resulting from this procedure are the maximum likelihood estimates.

The maximum likelihood estimator also provides a measure of the reliability of each estimate based on the information from each dynamic maneuver. This measure of the reliability, analogous to the standard deviation, is called the Cramér-Rao bound (refs. 13 and 15). The Cramér-Rao bound, as computed by current programs, should generally be used as a measure of relative, rather than absolute, accuracy. The bound is obtained from the approximation to the information matrix, \mathbf{H} , which is based on equation (11); the actual information matrix is defined when evaluated at the correct values (not the maximum likelihood estimates) of all the coefficients. The bound for each unknown is the square root of the corresponding diagonal element of \mathbf{H}^{-1} ; that is, for the i th

unknown, the Cramér-Rao bound is $\sqrt{(\mathbf{H}_{i,i}^{-1})}$. The stability and control derivatives presented and discussed in the next section were analyzed assuming that state noise was present in all cases.

RESULTS AND DISCUSSION

To accurately interpret the stability and control derivative results obtained here for the F-18, a careful examination of the quality and characteristics of the PID maneuvers themselves is necessary.

Parameter Identification Maneuvers

As mentioned in the previous section, two main difficulties affected the PID maneuvers and their analysis. The first issue was one of aerodynamics, resulting from unsteady separated and vortical flows over the aircraft above 20° AOA, which caused the aircraft to exhibit uncommanded motions of varying amplitude and frequency. The effect of the uncommanded responses was accounted for by considering state noise in the analysis.

The other difficulty arose because the PID maneuvers were performed with the basic F-18 control system engaged. The resulting maneuvers were less than ideal for derivative extraction because of the near linearly dependent (ref. 10) motions of all of the controls (especially above 25° AOA) and the relatively high correlation between the response variables and the resulting control motions due to the feedback control system.

The near linearly dependent control motions not only made it difficult to obtain control derivatives of individual control surfaces but also degraded attempts to determine an equivalent combined control derivative. In other words, the control deflections were too closely correlated to obtain good independent estimates of the correlated control deflections. Furthermore, this correlation made the attempt to estimate an equivalent control derivative—that is, a combination of two or more controls—also less than completely satisfactory. Correlations between response and control motions also made it difficult to obtain high-quality rate derivatives. These important issues will now be discussed more fully in connection with figures 4 through 7.

Figure 4 shows a typical maneuver obtained between 9° and 12° AOA. The altitude was about 31,000 ft at a Mach number of 0.46 to 0.41, with a dynamic pressure that varied between 88 and 72 lb/ft², as shown in figure 4(a). Figure 4(b) shows most of the responses and control inputs used for PID analysis. Figure 4(c) shows the pilot inputs made for the PID maneuver, along with the resulting control deflections. The control deflections are a result of the pilot input and the control command from the feedback control system. References 16 through 18 provide a more complete description of the control system. The lateral stick input δ_{a_p} , during the first 2 sec of the maneuver, directly causes deflections of δ_a , δ_{dh} , and δ_r in this portion of the maneuver. Fortunately in this maneuver, the pilot rudder input observed between 4 and 9 sec caused no deflection of the aileron and differential stabilator. (The aileron deflection between 7 and 9 sec is from pilot aileron input.) The result of this independent control surface motion is that a useful estimate of a combined δ_a and δ_{dh} effectiveness can be obtained independent of the δ_r effectiveness.

The first 2 sec of the maneuver are repeated in figure 4(d) on a finer scale. The response of the rudder and aileron shows that although both rudder and aileron respond to the pilot lateral stick input, the rate limiting of the rudder surface makes separation of δ_a and δ_r control effectiveness probable, which enhances the information from the rudder-pedal-pulse portion of the maneuver last discussed for figure 4(c). The difficulty of separating δ_a from δ_{dh} effectiveness can be seen by observing the high correlation (a multiple of 0.42) between δ_a and δ_{dh} . These control signals are essentially the same, except for a time lag of about 35 msec for the δ_{dh} signal compared with the δ_a signal. The high correlation (or near linear dependence (ref. 10)) between δ_a and δ_{dh} resulted in very poor estimates for δ_a

and δ_{dh} effectiveness; so the PID results for δ_a and δ_{dh} given here are for an equivalent combined lateral control defined as δ_L . Above 15° AOA, the coefficients of rolling moment due to lateral control, yawing moment due to lateral control, and lateral force due to lateral control are, respectively:

$$C_{l_{\delta_L}} = C_{l_{\delta_a}} + 0.42 C_{l_{\delta_{dh}}} \quad (12)$$

$$C_{n_{\delta_L}} = C_{n_{\delta_a}} + 0.42 C_{n_{\delta_{dh}}} \quad (13)$$

$$C_{Y_{\delta_L}} = C_{Y_{\delta_a}} + 0.42 C_{Y_{\delta_{dh}}} \quad (14)$$

The wind-tunnel predictions of $C_{l_{\delta_L}}$, $C_{n_{\delta_L}}$, and $C_{Y_{\delta_L}}$, to be used for comparison with flight-estimated values, are calculated with the same preceding equations. Between 2° and 15° AOA, the coefficients $C_{l_{\delta_L}}$, $C_{n_{\delta_L}}$, and $C_{Y_{\delta_L}}$ are nonlinear functions of δ_a , δ_{dh} , and δ_{TEF} controls. Figures 5 and 6 highlight the issues of correlation and linear dependency between differential control surface deflections. Figure 5 shows the relationship between pilot input and the resulting control surface deflections for full lateral stick input δ_{a_p} as a function of AOA; figure 6 shows them for full rudder input δ_{r_p} as a function of AOA.

For the maneuver shown in figure 4 at about 10° AOA, the resulting response to full δ_{a_p} , as given in figure 5, involves no deflection of differential trailing-edge flaps or differential leading-edge flaps. For the same maneuver, however, full δ_{a_p} results in about 23° of aileron deflection, 30° of rudder deflection, and 9° of differential stabilator deflection. Above 2° AOA, the differential leading-edge flap does not respond to δ_{a_p} , and above 10° AOA, differential trailing-edge flaps do not respond to δ_{a_p} . All maneuvers analyzed in this report are above 2° AOA, so no effect of differential leading-edge flap resulted. For the maneuvers below 10°, however, δ_{a_p} resulted in effects of trailing-edge flaps in addition to the effect of δ_a , δ_{dh} , and δ_r , as previously observed and discussed for figure 4.

Figure 6 shows the control deflections resulting from full rudder pedal deflection δ_{r_p} . Below 10° AOA, only the rudder deflects, but above 10° AOA, rudder, aileron, and differential stabilator all respond to pilot rudder pedal command. By comparing figures 5 and 6 above 25° AOA, one can see that rudder, aileron, and differential stabilator all respond to δ_{a_p} and δ_{r_p} with exactly the same proportions, making accurate estimation of the control effectiveness for δ_a , δ_{dh} , and δ_r difficult. The following discussion will examine a PID maneuver at a higher AOA. Not only are there differences in control deflections for given stick and rudder inputs (i.e., different control laws and scheduling), but there are also differences in flight dynamics due to unsteady aerodynamics.

Figure 7 shows a typical maneuver flown at AOA between 31° and 33°. For this maneuver, the altitude is between 16,000 and 15,300 ft, the Mach number is from 0.23 to 0.22, and the dynamic pressure varies from 42 to 40 lb/ft². Figure 7(b) shows the response variables and control inputs used for PID. Figure 7(c) shows the pilot inputs δ_{a_p} and δ_{r_p} , along with the resulting deflections of δ_a , δ_{dh} , and δ_r . During the first 2 sec, the pilot rudder pedal input δ_{r_p} can be seen with very little pilot lateral stick input. The resulting deflections for δ_a , δ_{dh} , and δ_r can be seen. These deflections are different from those for the lower AOA maneuver that figure 4 shows where δ_{r_p} only results in δ_r deflection. Near 17 sec, the pilot lateral stick input can be seen along with the resulting deflections of δ_a , δ_{dh} , and δ_r . The amount of control surface deflection due to δ_{a_p} and δ_{r_p} is the same in this AOA range as would be expected by comparing figures 5 and 6.

The correlation of δ_a , δ_{dh} , and δ_r with δ_{r_p} is more apparent in figure 7(d), where the first 2 sec of the maneuver are shown on a more sensitive scale. Once again, δ_a is highly correlated with 0.42 δ_{dh} , and δ_r is seen to be about

four times $-\delta_a$. Fortunately, the rate limit in the δ_r surface, seen in figure 7(d), should result in some linear independence between δ_a and δ_r , which will allow, however marginally, an estimate of δ_a and δ_{dh} effects (through δ_L) independent from δ_r effects, in the PID analysis.

Figure 7(e) shows the high-AOA maneuver at an increased time sensitivity between 17 and 19 sec. Here the deflection of the controls δ_a , δ_{dh} , and δ_r are shown for the pilot lateral stick input δ_{a_p} . Once again, the previously observed correlation between δ_a and δ_{dh} can be seen. The rate limit saturation of δ_r here shows limited independence between δ_a and δ_r for PID purposes.

With this discussion considered, the PID results that follow will estimate rudder derivatives independent of the equivalent lateral control variable δ_L as previously defined.

Extracted Stability and Control Derivatives

All lateral-directional maneuvers were analyzed using the maximum likelihood method with state noise as described in the “Parameter Identification Methodology” section. State noise was assumed for all maneuvers regardless of AOA, although the uncommanded responses warranting use of state noise were only significant above 20° AOA. The lateral-directional derivative estimates are presented as functions of AOA in figures 8 through 11, along with corresponding wind-tunnel predictions. The circle indicates the estimate of each derivative from a given flight maneuver, with the vertical bar indicating the uncertainty level for the estimate. The uncertainty level used in this analysis is five times the Cramér-Rao bound. The solid line is a fairing of the estimates without any consideration of the wind-tunnel values and represents the authors’ interpretation of the estimate, which includes a combined assessment of the uncertainty levels, the scatter in the estimates, and the quality of the individual maneuver. In addition to the issues of near-linear dependence discussed previously, the authors also assessed the maneuvers on the basis of the duration of the maneuver, the amount of control input, and the level of excitation of the vehicle (response variables β , p , r , and a_Y). Theoretically, these considerations are also contained in the values of the uncertainty levels, where a large uncertainty level indicates low information on that derivative, and a small value indicates high information. The dashed line shown on the figure represents the wind-tunnel prediction of the derivatives as a function of AOA. The predictions are from the aerodynamic model and database used in the DFRC flight simulator of the F-18 aircraft. The aeromodel was acquired from the U.S. Navy Naval Air Test Center, Patuxent River, Maryland, and based on the McDonnell Douglas F-18 basic aerodynamic database (refs. 19 and 20). Although the flight estimated stability and control derivatives are plotted as functions of AOA, other variables, such as altitude (and thus Reynolds number) and horizontal stabilator position, account for some of the scatter in the flight estimates seen in these figures.

Figure 8 shows the sideslip derivatives C_{l_β} , C_{n_β} , and C_{Y_β} as functions of AOA. The comparison between flight estimate and wind-tunnel prediction of C_{l_β} (dihedral) in figure 8(a) is very good below 20° AOA. The flight fairing is up to 0.001 more positive than the wind-tunnel prediction between 20° and 25° AOA and up to 0.0015 more negative between 25° and 42° AOA. The flight and wind-tunnel values are in very good agreement above 42° AOA. To assess the agreement between 33° and 42° AOA is difficult, as only two maneuvers are in this interval, both with fairly large uncertainty levels. More flight maneuvers in this interval would be required to make a definitive statement about the correlation of flight estimates and wind-tunnel predictions of C_{l_β} between 33° and 42° AOA.

Flight-estimated and wind-tunnel trends of C_{n_β} (directional stability) with AOA are very similar, as figure 8(b) shows. In general, the flight trend is somewhat lower below an AOA of 10°. At 20° AOA and above, the wind-tunnel prediction is a very valid fairing of the flight estimates, indicating excellent agreement between flight estimate and wind-tunnel predictions.

Figure 8(c) shows C_{Y_β} as a function of AOA for both flight estimates and wind-tunnel predictions where the flight values are consistently higher below an AOA of 25° and between 35° and 45°. The paucity of maneuvers between AOA of 33° and 42° makes derivative assessment in this region difficult.

Figure 9 shows flight estimates and wind-tunnel predictions for the equivalent combined lateral control derivatives ($C_{l_{\delta_L}}$, $C_{n_{\delta_L}}$, and $C_{Y_{\delta_L}}$) as functions of AOA. Above 15° AOA, both extracted and predicted lateral control derivatives are as previously defined:

$$C_{l_{\delta_L}} = C_{l_{\delta_a}} + 0.42 C_{l_{\delta_{dh}}}$$

$$C_{n_{\delta_L}} = C_{n_{\delta_a}} + 0.42 C_{n_{\delta_{dh}}}$$

$$C_{Y_{\delta_L}} = C_{Y_{\delta_a}} + 0.42 C_{Y_{\delta_{dh}}}$$

Below 15° AOA, flight estimates and fairings are given, but wind-tunnel predictions are not assumed in this range because of more complicated control surface correlations and dependencies. The trend of the lateral control effectiveness $C_{l_{\delta_L}}$ for both flight estimates and wind-tunnel predictions in figure 9(a) is the same. The agreement varies, with the flight estimate showing 10 to 30 percent more effectiveness. In figure 9(b), the decreasing trend of $C_{n_{\delta_L}}$ as a function of AOA is seen for both flight and prediction up to an AOA of 35°. The flight values are more proverse (more positive $C_{n_{\delta_L}}$) than prediction for all AOA, with the flight values showing a trend toward even more proverse values above 30° AOA. Figure 9(c) shows that the $C_{Y_{\delta_L}}$ is very small for both flight and prediction.

Figure 10 shows the rudder derivatives as functions of AOA. Figure 10(a) shows $C_{l_{\delta_r}}$ as a function of AOA for flight and predicted values. Flight and predicted values agree below an AOA of 25°, and then flight values increase up to 0.0005 more positive than the wind-tunnel prediction above 25° AOA. The rudder effectiveness $C_{n_{\delta_r}}$ (fig. 10(b)), shows good agreement throughout the AOA range, but the flight values indicate somewhat more effectiveness below 25° AOA than the predicted values. The agreement between flight and predicted values for $C_{Y_{\delta_r}}$ for all AOA is excellent (fig. 10(c)).

Figure 11 compares flight and predicted values of the rotary derivatives C_{l_p} , C_{n_p} , C_{l_r} , and C_{n_r} as functions of AOA. The flight values of C_{l_p} (fig. 11(a)) are closer to zero than predicted near 20° AOA and between 30° and 45° AOA. The flight values of C_{l_r} (fig. 11(b)) are near zero for most of the AOA range, dipping negatively near 32° AOA, while the predicted values remain positive over the entire AOA range. Figure 11(c) compares C_{n_p} flight values and prediction with AOA, and the prediction is near zero throughout. Figure 11(d) compares flight and predicted values for C_{n_r} , with good agreement below 20° AOA. Above 20° AOA, the flight values are more positive than the predicted values. It is always difficult to obtain linear rate derivatives at high AOA, but it is especially so for the maneuvers analyzed here. These maneuvers were obtained with the rate feedback control system engaged, and they also suffered because of the high correlation (discussed earlier) of the control surfaces used in the feedback control system.

CONCLUDING REMARKS

The lateral-directional stability and control derivatives of an F-18 research aircraft were extracted from flight data over an angle-of-attack range of 3° to 47° using a maximum likelihood estimator accounting for state and measurement noise. The F-18 testbed performed these parameter identification flight maneuvers between June 1987

and March 1988 in its basic hardware and software configuration. The lateral-directional maneuvers were less than ideal for parameter identification because of high correlations between different control surfaces and because of control system inputs by the rate feedback control system, hindering the assessment of individual control effectiveness. In addition, uncommanded aircraft motions were involved above 20° angle of attack because of unsteady aerodynamics, such as separated and vortical flows, over the aircraft. State noise was used to model this uncommanded forcing function.

Two maneuvers, one near 10° and the other near 32° angle of attack, were examined in detail, underscoring the difficulties introduced by the F-18 control system (e.g., the aileron-to-rudder and rudder-to-aileron interconnects) in response to lateral stick inputs and rudder inputs. Because of near linear dependency problems between the aileron and differential stabilator control surfaces, an equivalent lateral control δ_L was defined to denote a combined aileron and differential stabilator control.

Despite the degraded maneuvers, lateral-directional stability and control derivatives (C_{l_β} , C_{n_β} , C_{Y_β} , $C_{l_{\delta_L}}$, $C_{n_{\delta_L}}$, $C_{Y_{\delta_L}}$, $C_{l_{\delta_r}}$, $C_{n_{\delta_r}}$, $C_{Y_{\delta_r}}$, C_{l_p} , C_{l_r} , C_{n_p} , and C_{n_r}) were estimated, plotted, and compared with wind-tunnel predictions. The coefficients of yawing moment due to sideslip (C_{n_β}) and lateral force due to sideslip (C_{Y_β}) exhibited good comparison with wind-tunnel prediction, capturing predominant trends over the entire angle-of-attack range. Estimated derivatives for the equivalent lateral control were fair. The rudder derivatives showed fair comparison as well. The rotary derivatives exhibited largely poor correlation between flight estimate and prediction.

*Dryden Flight Research Center
National Aeronautics and Space Administration
Edwards, California, November, 1996*

REFERENCES

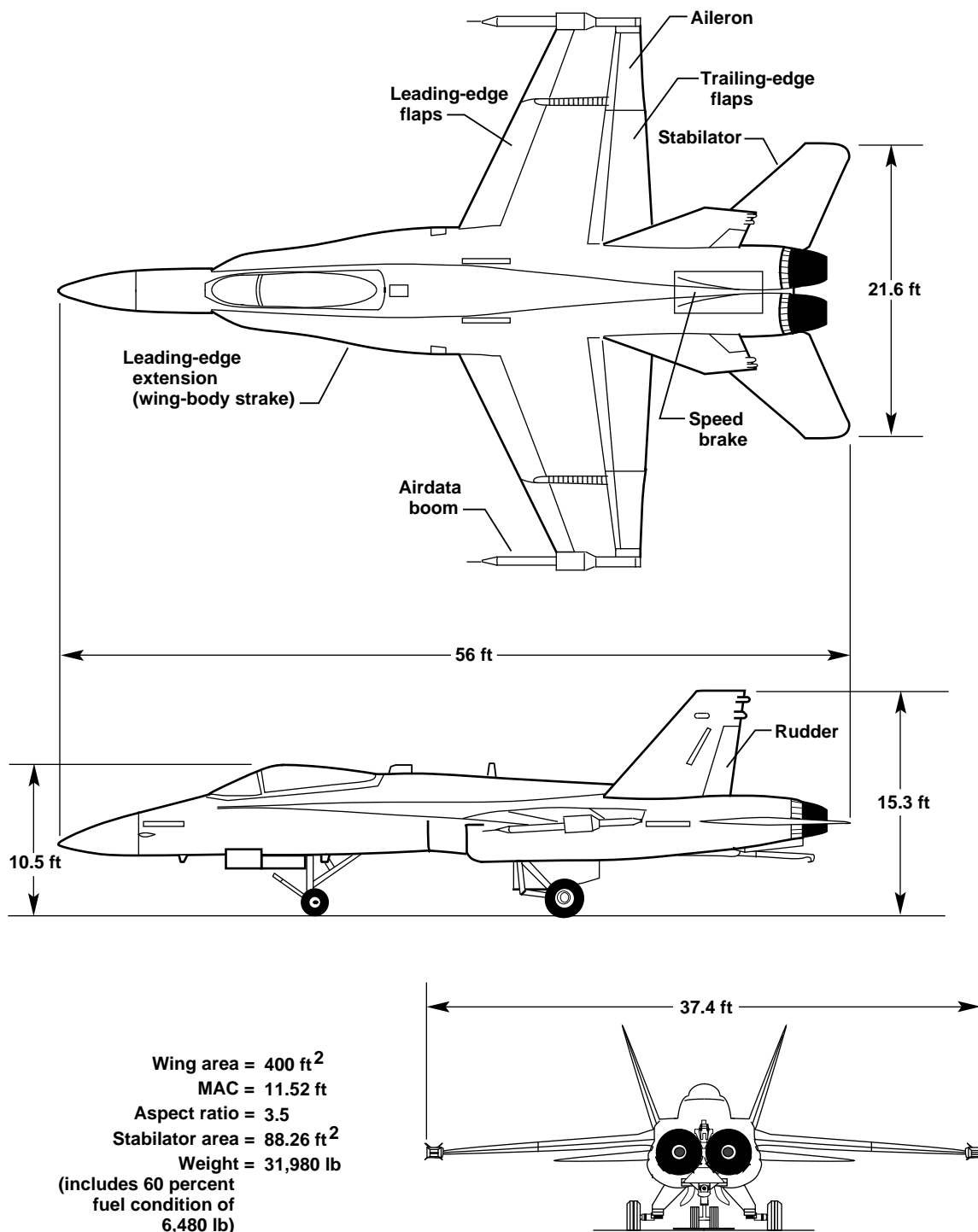
1. Gilbert, William P. and Donald H. Gatlin, "Review of the NASA High-Alpha Technology Program," *High-Angle-of-Attack Technology - Volume 1*, NASA CP-3149, Part 1, Joseph R. Chambers, William P. Gilbert, and Luat T. Nguyen, editors, Langley Research Center, Hampton, Virginia, May, 1992, pp. 23–59.
2. Klein, Vladislav, Thomas P. Ratvasky, and Brent R. Cobleigh, *Aerodynamic Parameters of High-Angle-of-Attack Research Vehicle (HARV) Estimated From Flight Data*, NASA TM-102692, Aug. 1990.
3. Klein, Vladislav, "Aerodynamic Characteristics of High-Angle-of-Attack Research Vehicle (HARV) Determined From Flight Data," *High-Angle-of-Attack Technology - Volume 1*, NASA CP-3149, Part 1, Joseph R. Chambers, William P. Gilbert, and Luat T. Nguyen, editors, Langley Research Center, Hampton, Virginia, Oct. 30 to Nov. 1, 1990, pp. 265–278.
4. Moes, Timothy R. and Stephen A. Whitmore, *A Preliminary Look at Techniques Used to Obtain Airdata From Flight at High Angles of Attack*, NASA TM-101729, Dec. 1990.
5. Whitmore, Stephen A., Timothy R. Moes, and Terry J. Larson, *Preliminary Results From a Subsonic High Angle-of-Attack Flush Airdata Sensing (HI-FADS) System: Design, Calibration, and Flight Test Evaluation*, NASA TM-101713, 1990 (also available as AIAA 90-0232, Jan. 1990).
6. Richwine, David M., Robert E. Curry, and Gene V. Tracy, *A Smoke Generator System for Aerodynamic Flight Research*, NASA TM-4137, Sept. 1989.
7. Fisher, David F., John H. Del Frate, and David M. Richwine, *In-Flight Flow Visualization Characteristics of the NASA F-18 High Alpha Research Vehicle at High Angles of Attack*, NASA TM-4193, May 1990.
8. Fisher, David F., David M. Richwine, and Daniel W. Banks, *Surface Flow Visualization of Separated Flows on the Forebody of an F-18 Aircraft and Wind-Tunnel Model*, NASA TM-100436, May 1988.
9. Fisher, David F. and Robert R. Meyer, Jr., *Flow Visualization Techniques for Flight Research*, NASA TM-100455, Oct. 1988.
10. Iliff, Kenneth W. and Richard E. Maine, *Practical Aspects of Using a Maximum Likelihood Estimation Method to Extract Stability and Control Derivatives From Flight Data*, NASA TN D-8209, Apr. 1976.
11. Iliff, Kenneth W., Richard E. Maine, and Mary F. Shafer, *Subsonic Stability and Control Derivatives for an Unpowered, Remotely Piloted 3/8-Scale F-15 Airplane Model Obtained From Flight Test*, NASA TN D-8136, Jan. 1976.
12. Iliff, Kenneth W., "Identification and Stochastic Control with Application to Flight Control in Turbulence," UCLA-ENG-7430, Ph.D. Dissertation, University of California, Los Angeles, California, May 1973.
13. Maine, R. E. and K. W. Iliff, *Identification of Dynamic Systems*, AGARD-AG-300-Vol. 2, Jan. 1985 (also available as NASA RP-1138, Feb. 1985).
14. Iliff, Kenneth W., "Identification and Stochastic Control of an Aircraft Flying in Turbulence," *Journal of Guidance and Control*, vol. 1, no. 2, March–April, 1978, pp. 101–108.
15. Iliff, Kenneth W. and Lawrence W. Taylor, Jr., *Determination of Stability Derivatives From Flight Data Using a Newton-Raphson Minimization Technique*, NASA TN D-6579, Mar. 1972.
16. Groll, D. B., R. K. Hess, W. D. Hodges, and R. F. Moomaw, "F/A-18A Flight Control System Design Report," Vols. I, II, and III, MDC A7813, rev. A, McDonnell Aircraft Co., McDonnell Douglas Corp., St. Louis, Missouri, Sept. 1984.

17. Moran, W. A., "Operational and Developmental Experience with the F/A-18A Digital Flight Control System," *Active Control Systems - Review, Evaluation and Projections*, AGARD Conference Proceedings No. 384, Flight Mechanics Panel Symposium, Toronto, Canada, October 15–18, 1984, pp. 12A 1–13.
18. Burton, R. A., B. T. Kneeland, U. H. Rabin, and R. S. Hansen, "Flight Testing and Development of the F/A-18A Digital Flight Control System," *Active Control Systems - Review, Evaluation and Projections*, AGARD Conference Proceedings No. 384, Flight Mechanics Panel Symposium, Toronto, Canada, October 15–18, 1984, pp. 12B 1–18.
19. Anon., "F/A-18 Basic Aerodynamic Data," MDC A8575, McDonnell Aircraft Co., McDonnell Douglas Corp., St. Louis, Missouri, 1984.
20. Pelikan, R. J. and R. L. Swingle, "F/A-18 Stability and Control Data Report," Vols. I and II, MDC A7247, rev. B, McDonnell Aircraft Co., McDonnell Douglas Corp., St. Louis, Missouri, Aug. 1981.



EC89 096-215

Figure 1. NASA F-18 High Angle-of-Attack Research Vehicle.



960825

Figure 2. Three-view of the F-18 with major dimensions shown.

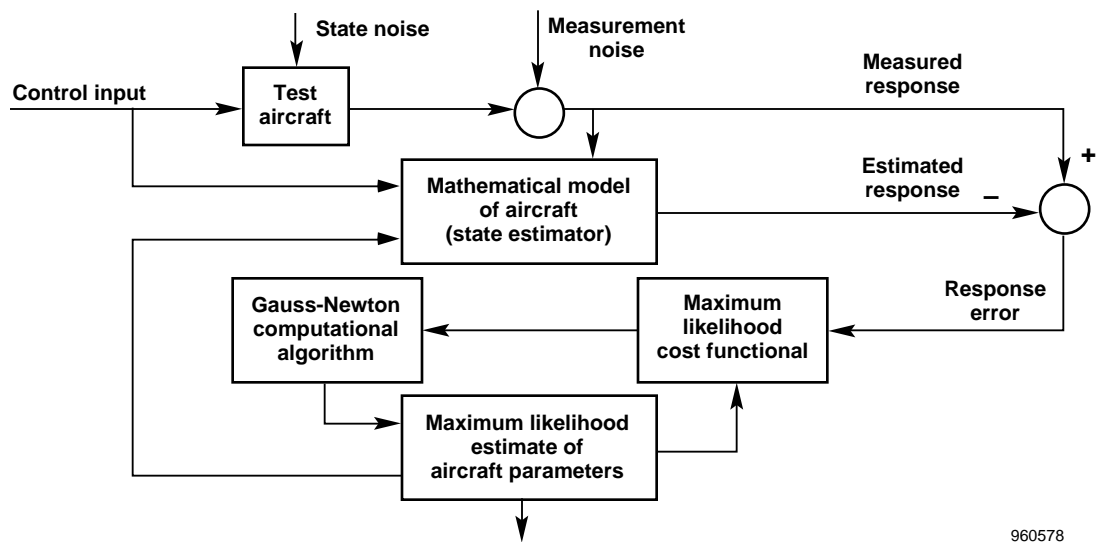
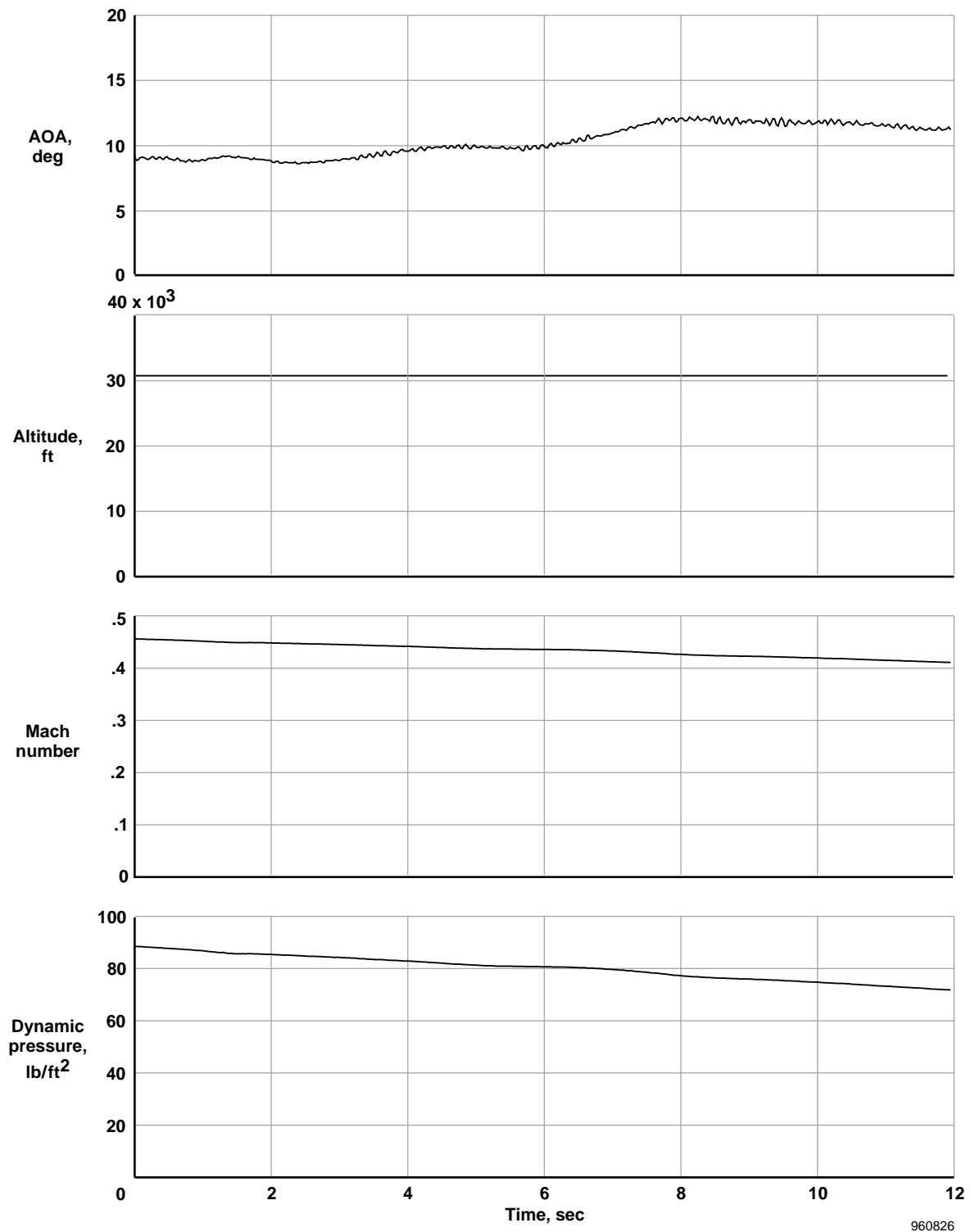
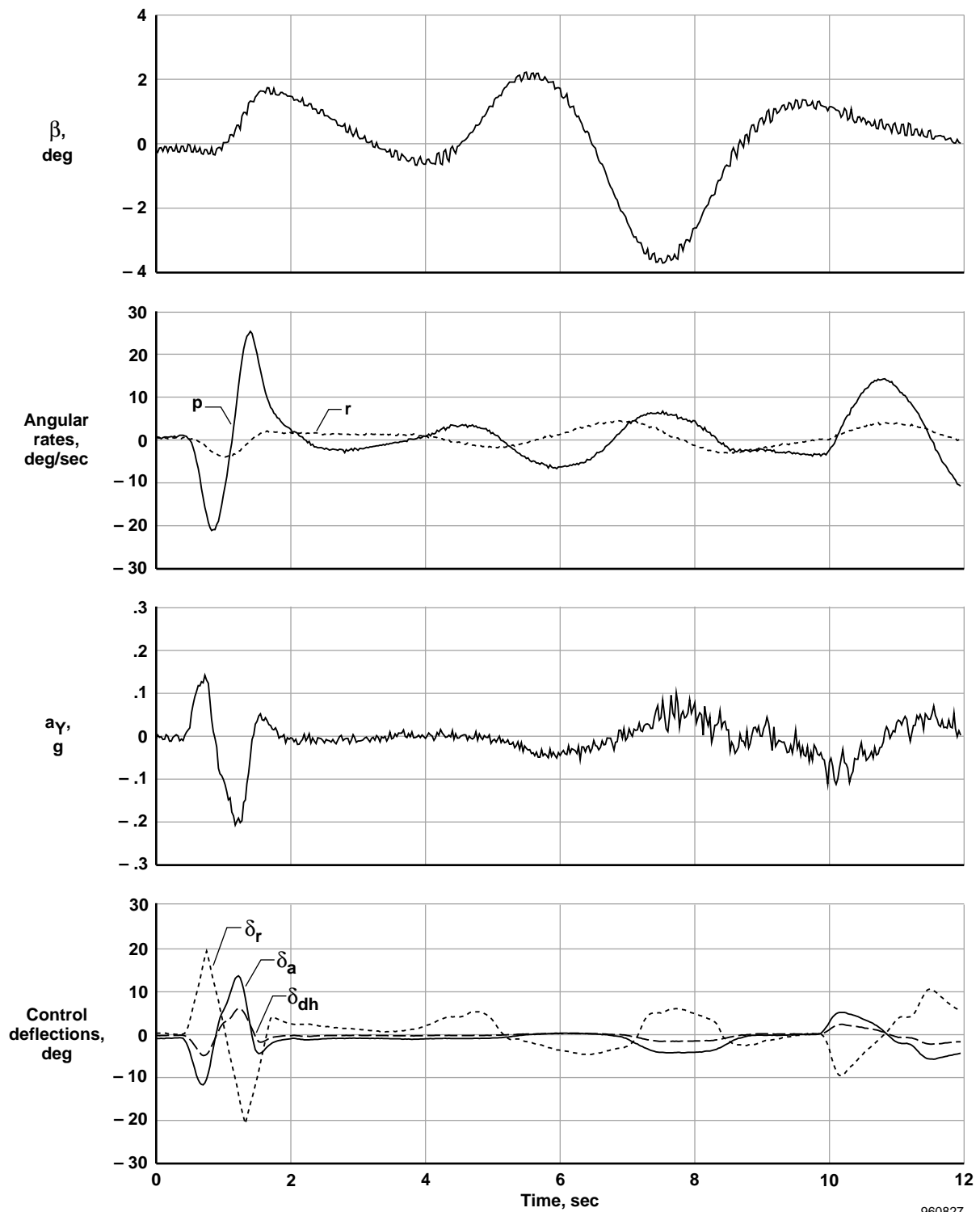


Figure 3. Maximum likelihood estimation concept with state and measurement noise.



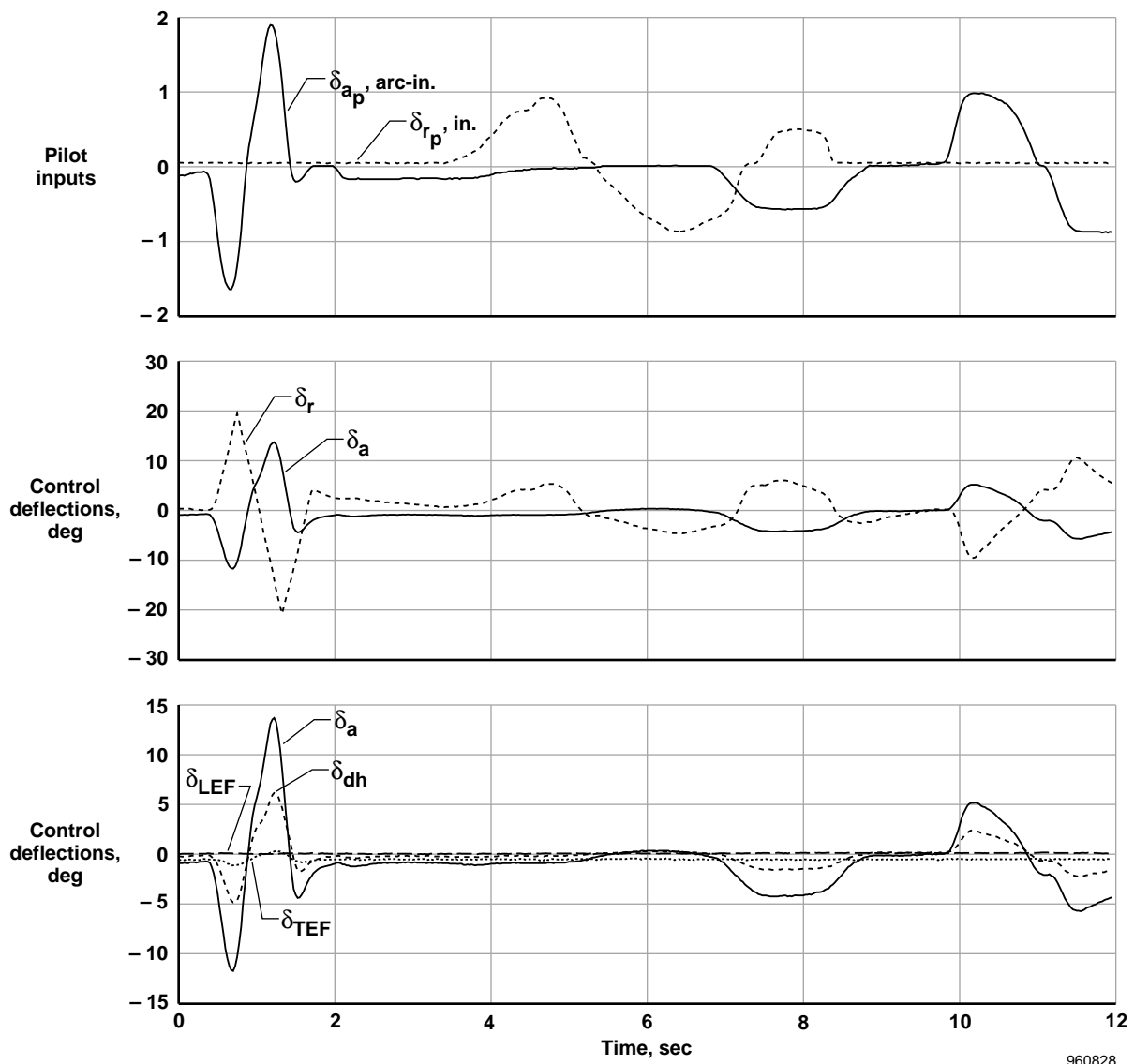
(a)

Figure 4. Time-history data from a typical lateral-directional PID maneuver at low AOA.



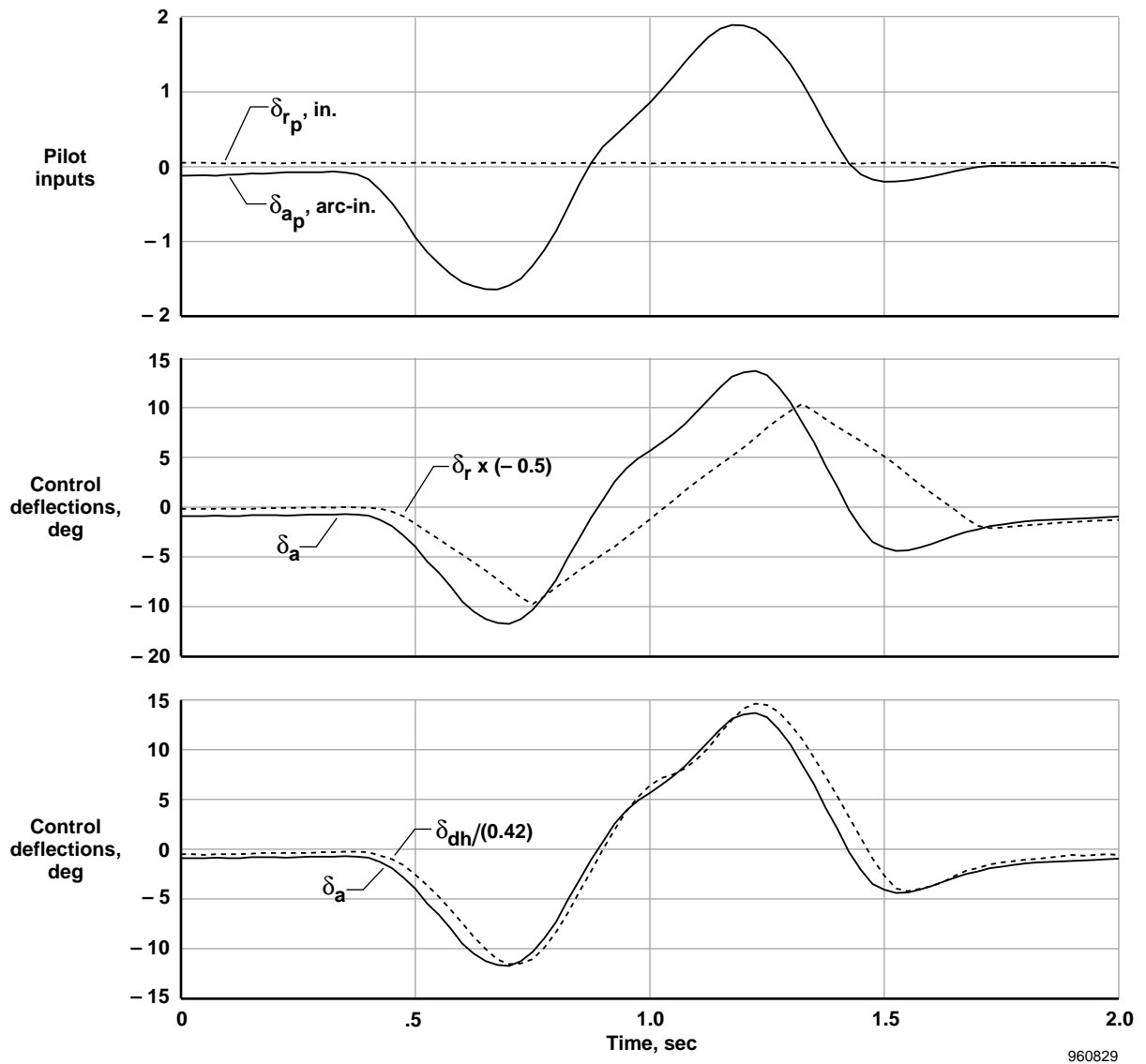
(b)

Figure 4. Continued.



(c)

Figure 4. Continued.



(d)

Figure 4. Concluded.

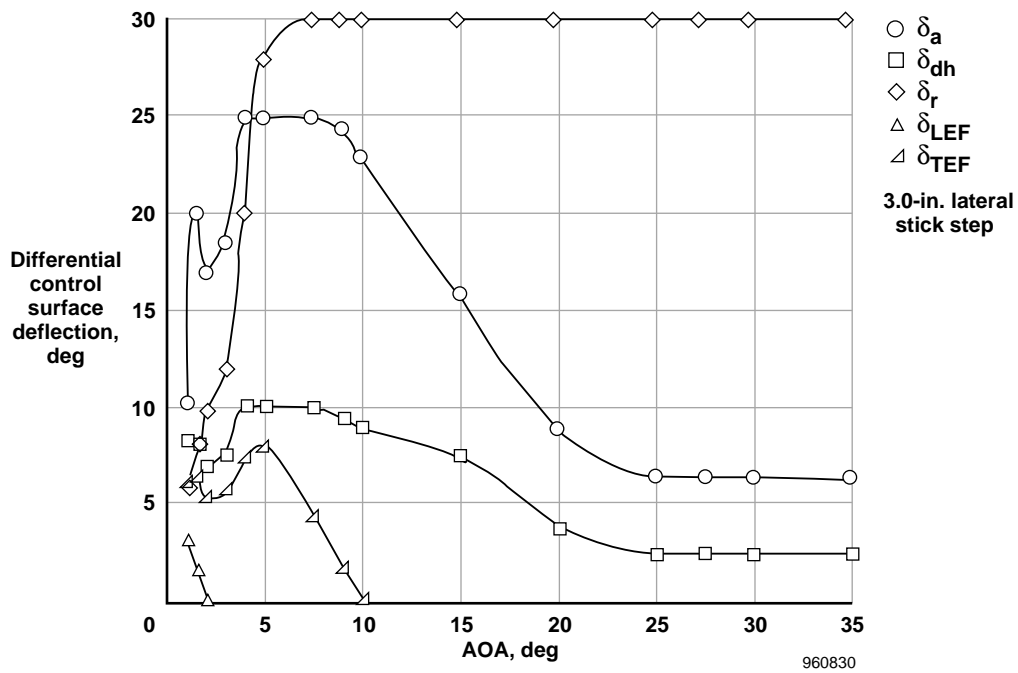


Figure 5. Differential control surface deflection schedule due to aileron input (with ARI).

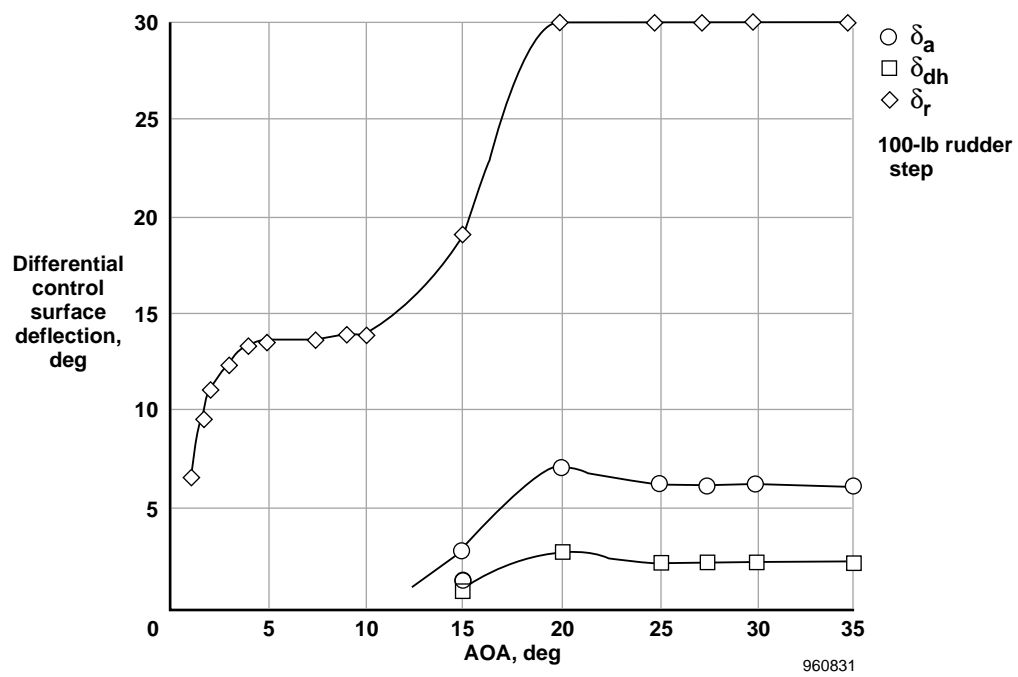
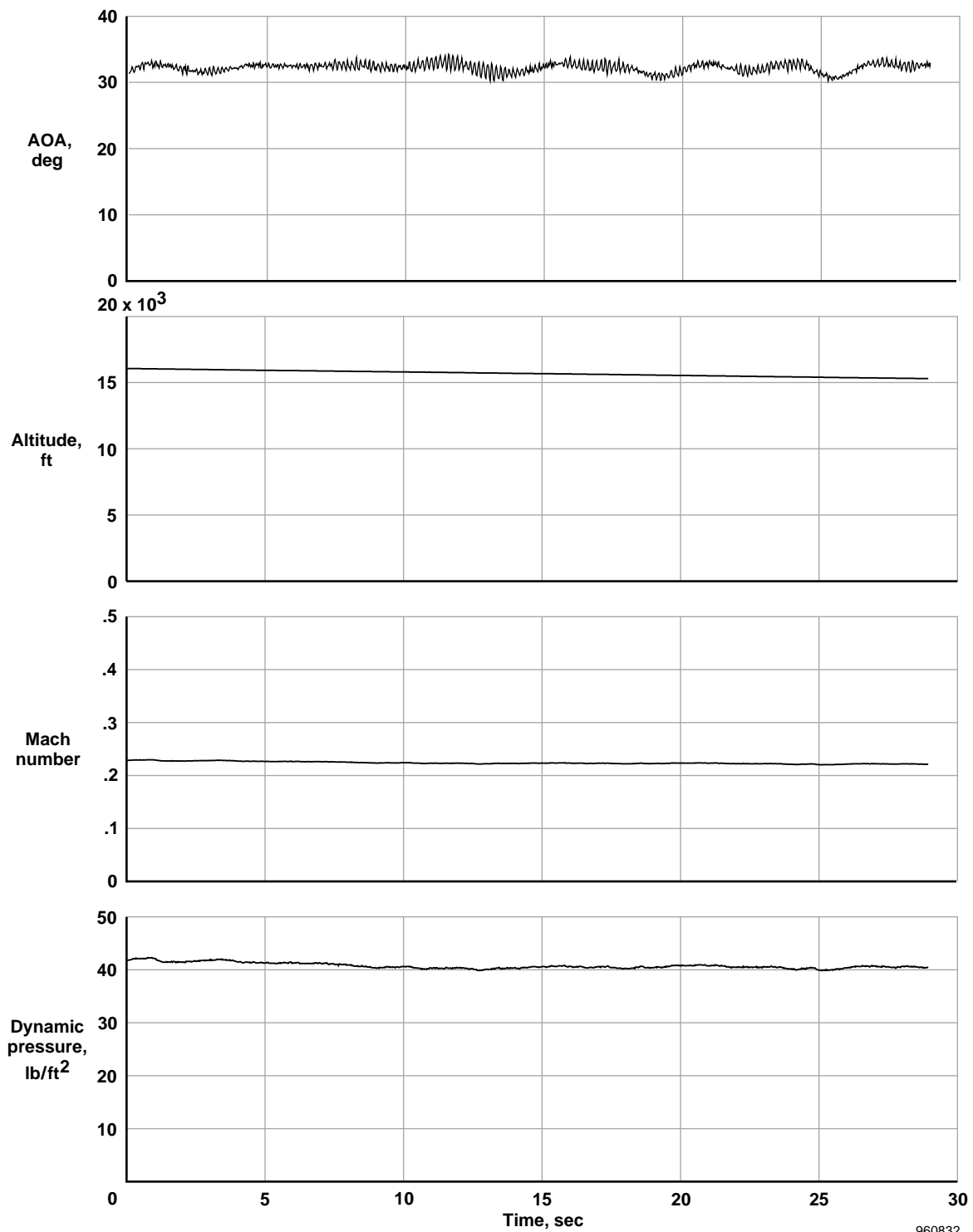
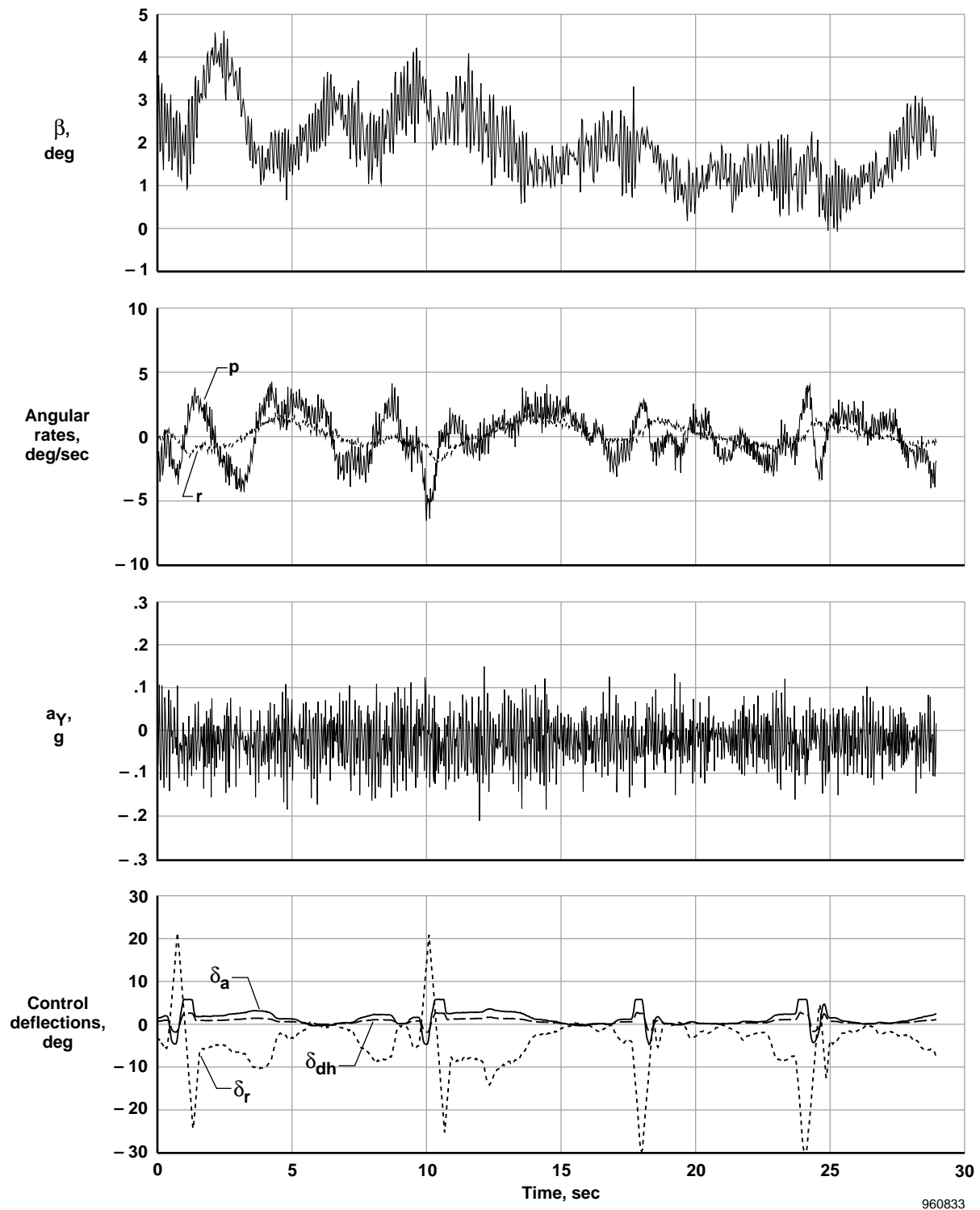


Figure 6. Differential control surface deflection schedule due to rudder input (with RAI).



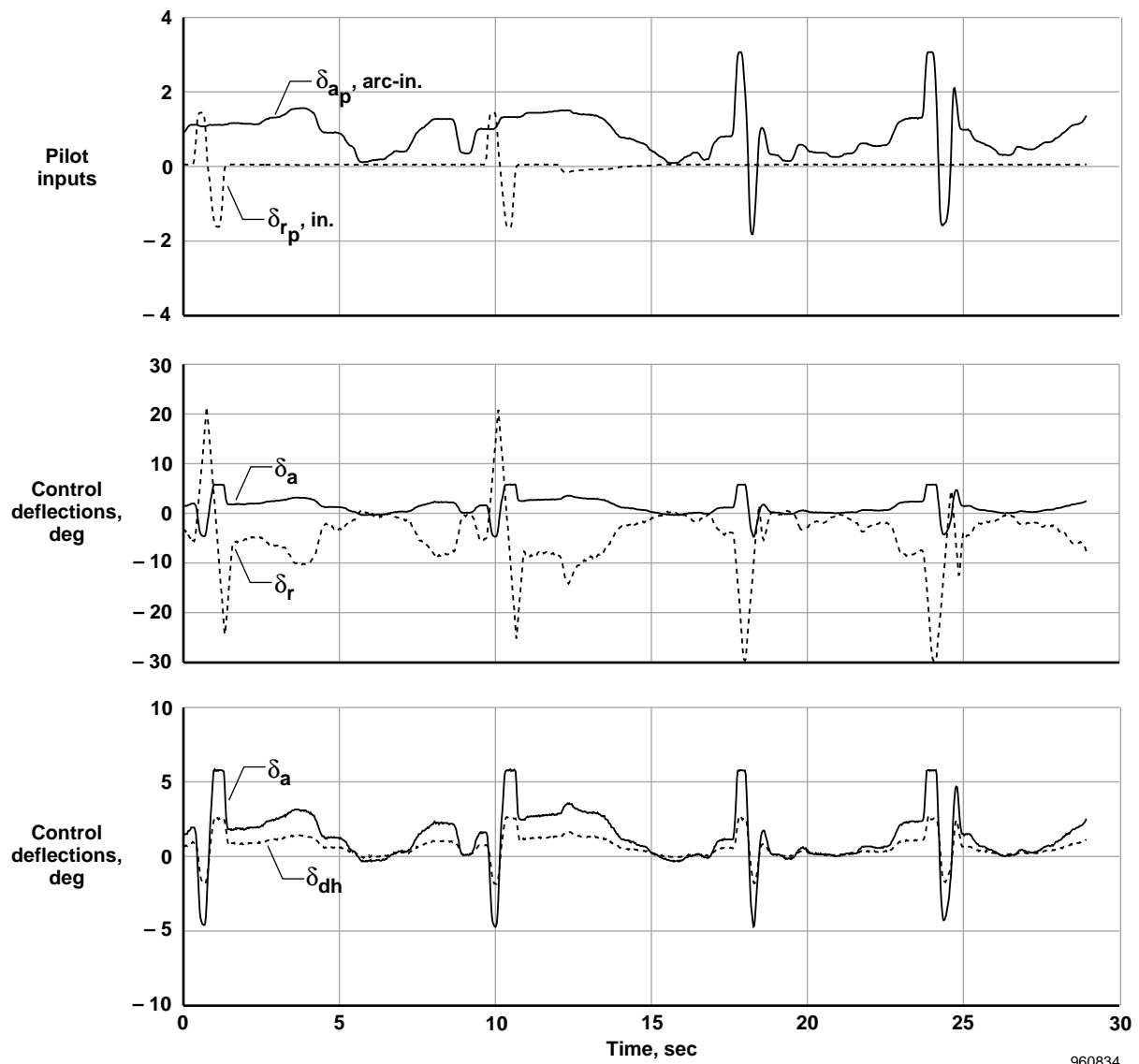
(a)

Figure 7. Time-history data from a typical lateral-directional PID maneuver at high AOA.



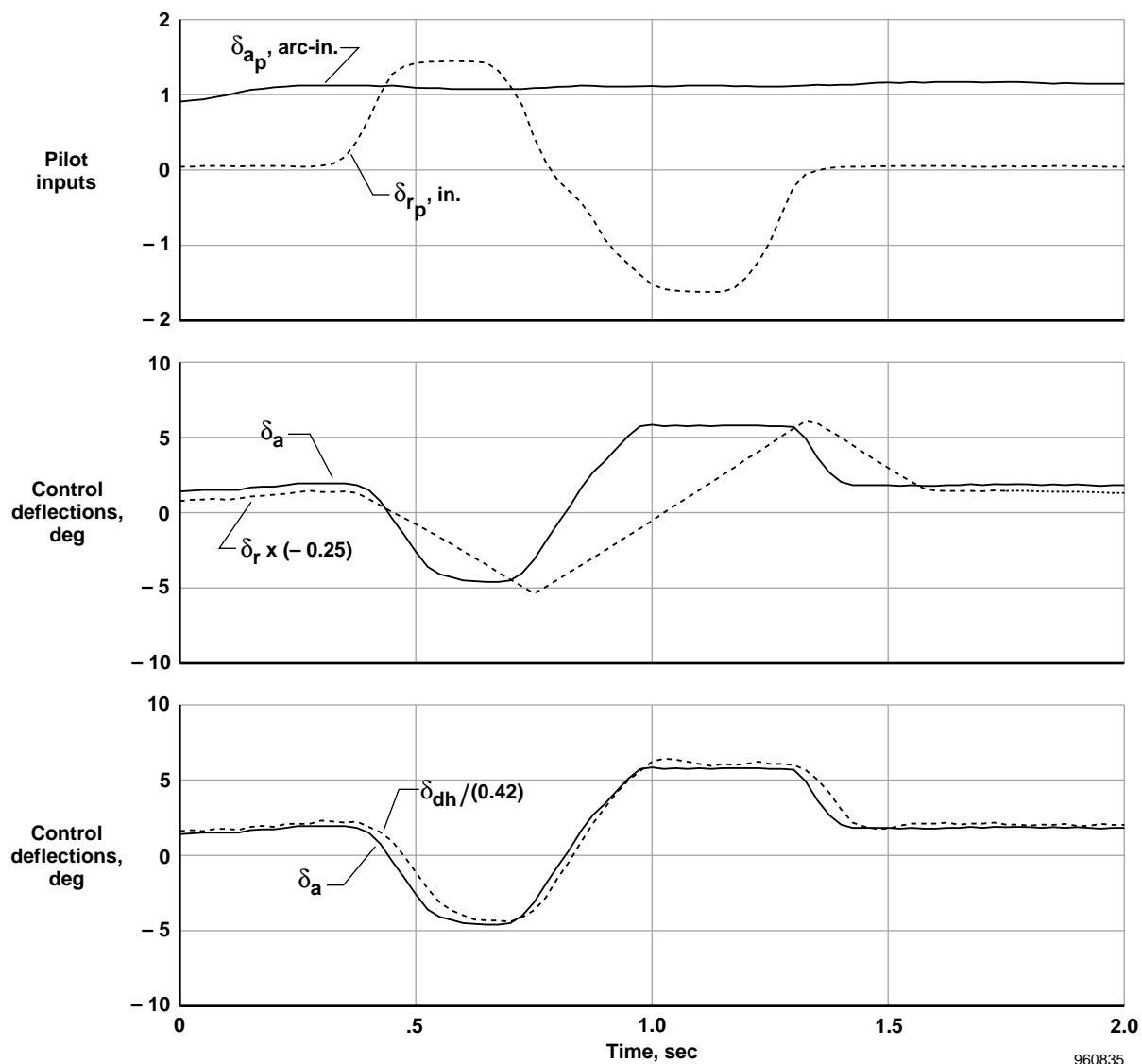
(b)

Figure 7. Continued.



(c)

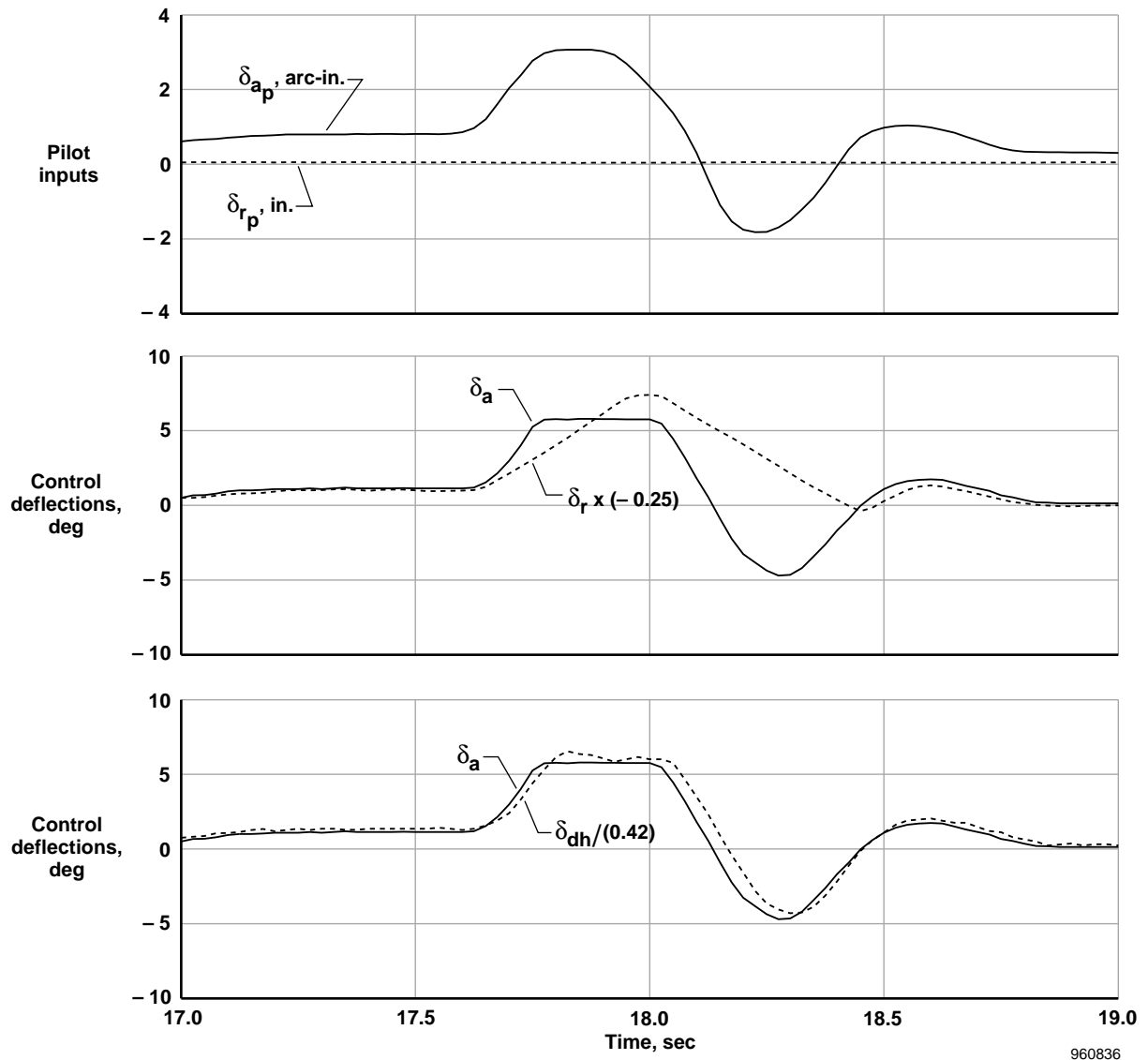
Figure 7. Continued.



960835

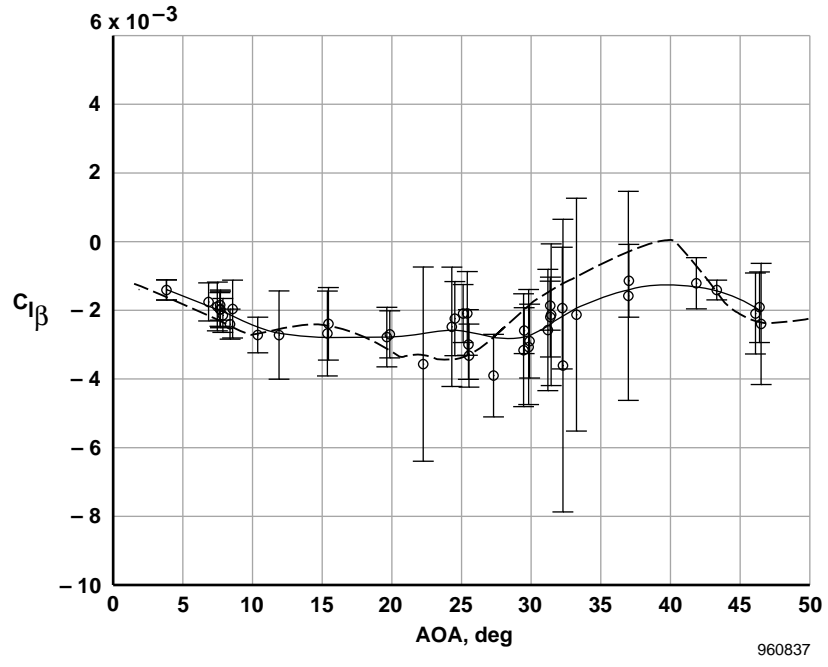
(d)

Figure 7. Continued.

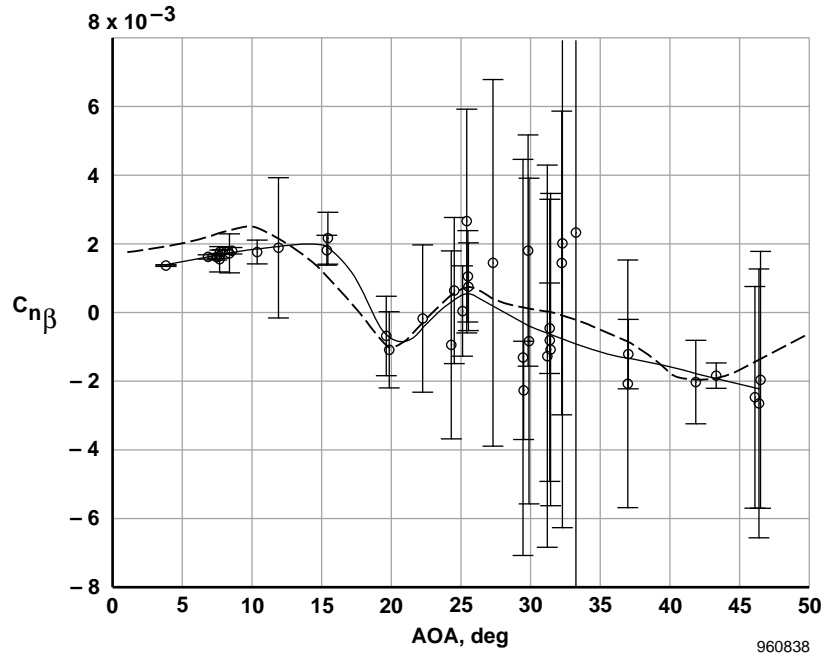


(e)

Figure 7. Concluded.

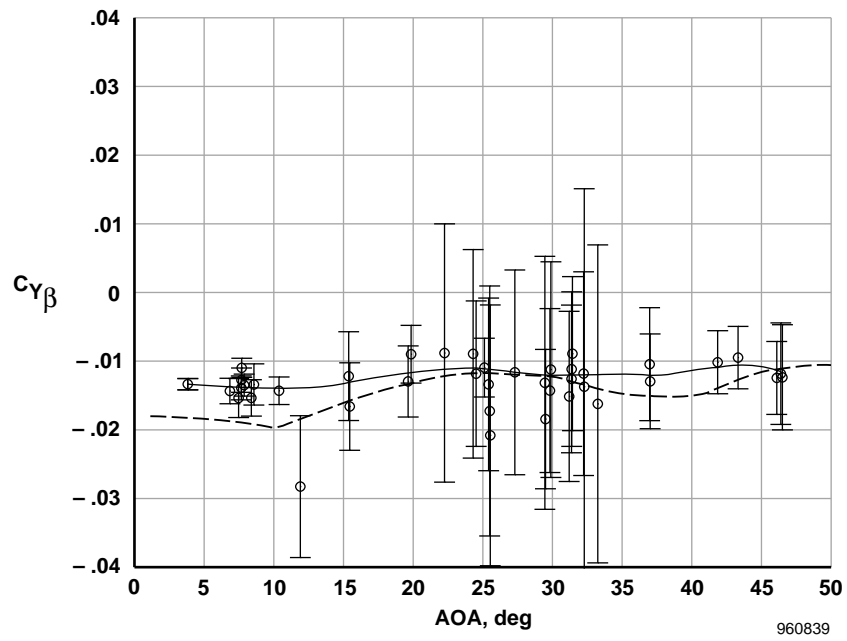


(a) C_{l_β} as a function of AOA.



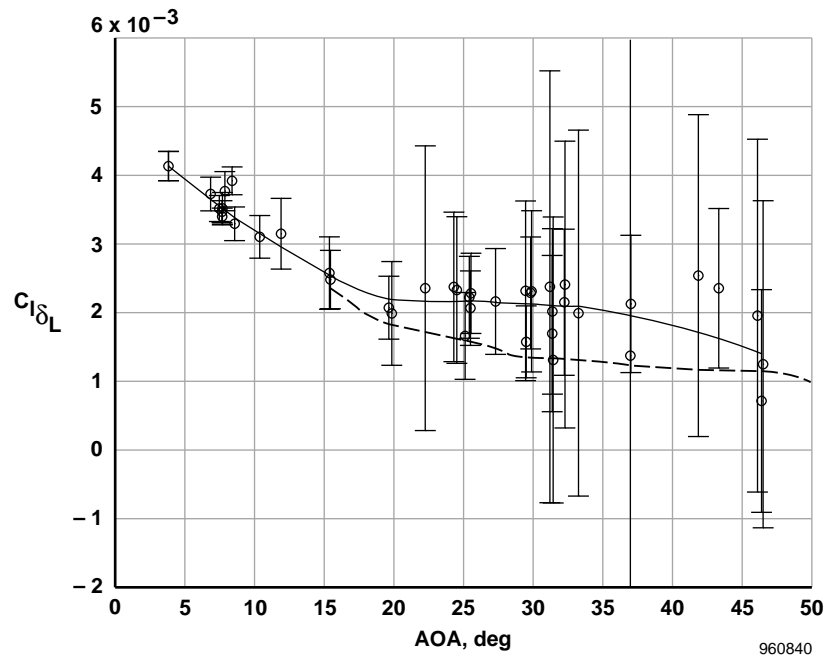
(b) C_{n_β} as a function of AOA.

Figure 8. Sideslip derivatives as functions of AOA.



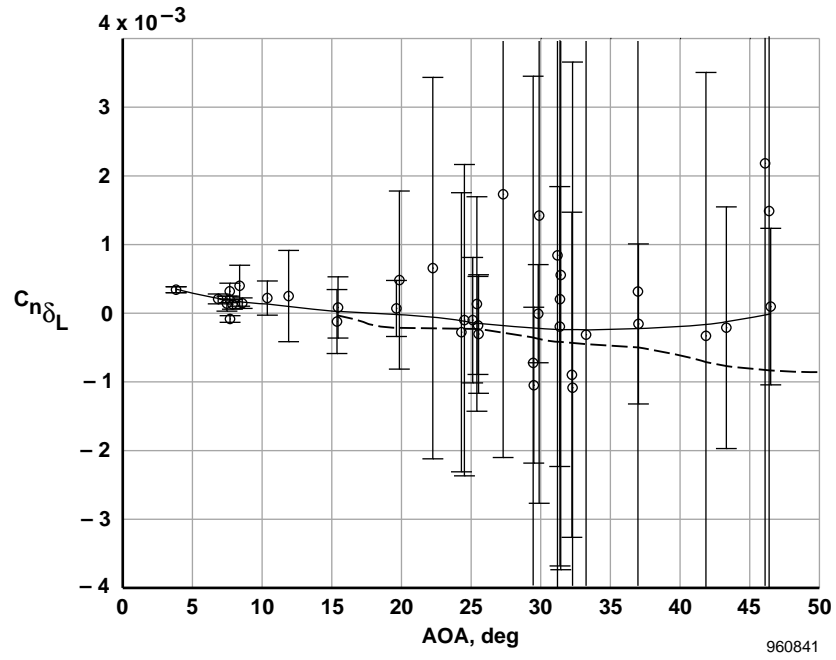
(c) C_{Y_β} as a function of AOA.

Figure 8. Concluded.

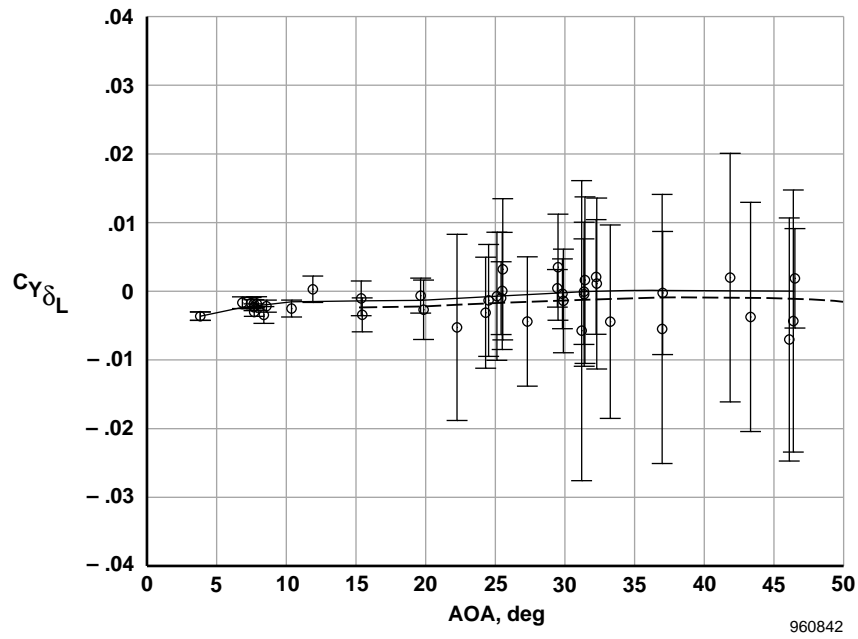


(a) $C_{l_{\delta_L}}$ as a function of AOA.

Figure 9. Equivalent lateral control derivatives as functions of AOA.

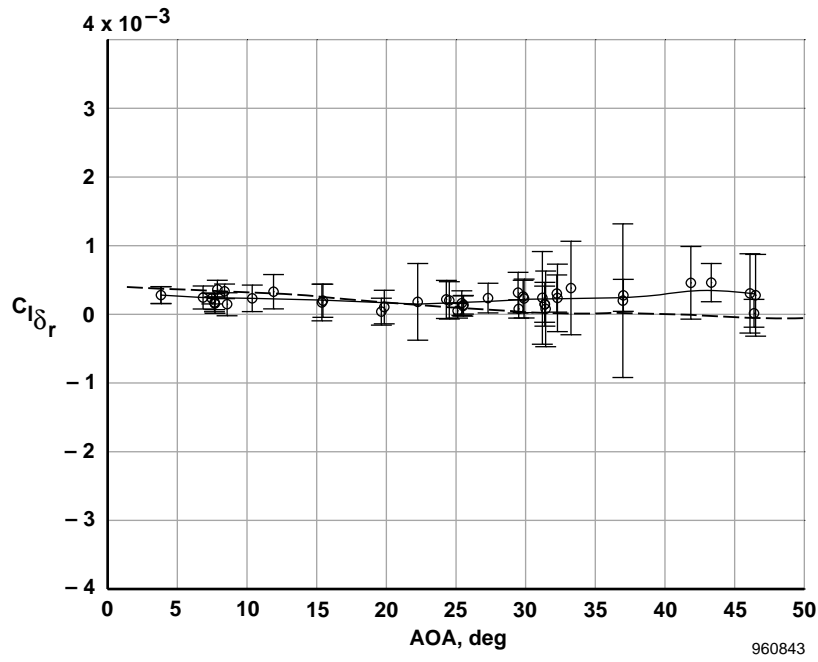


(b) $C_{n\delta_L}$ as a function of AOA.

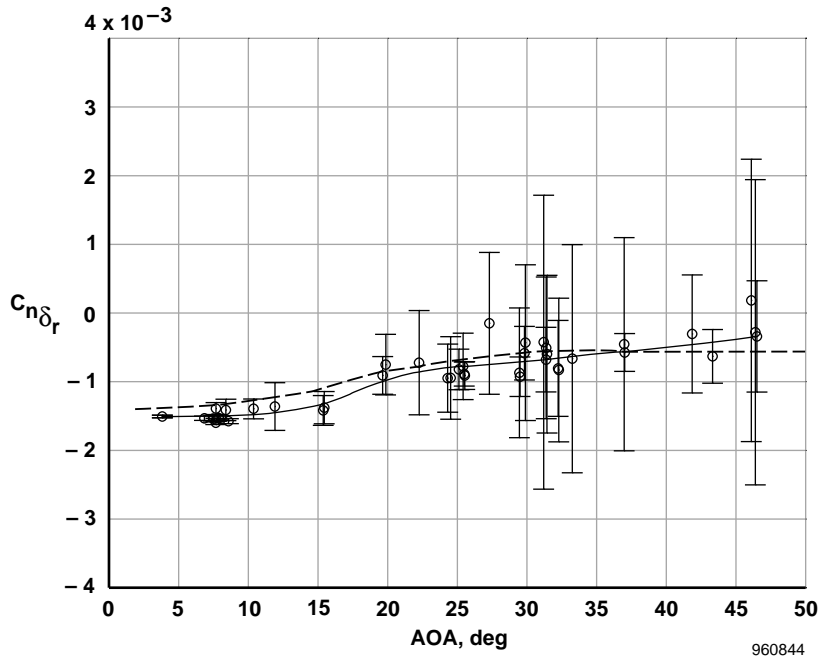


(c) $C_{Y\delta_L}$ as a function of AOA.

Figure 9. Concluded.

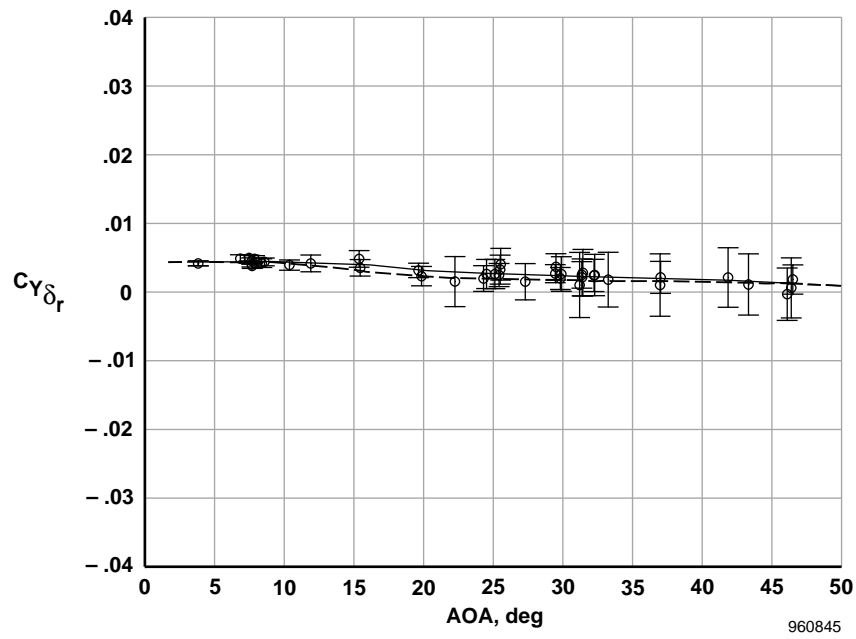


(a) $C_{l_{\delta_r}}$ as a function of AOA.



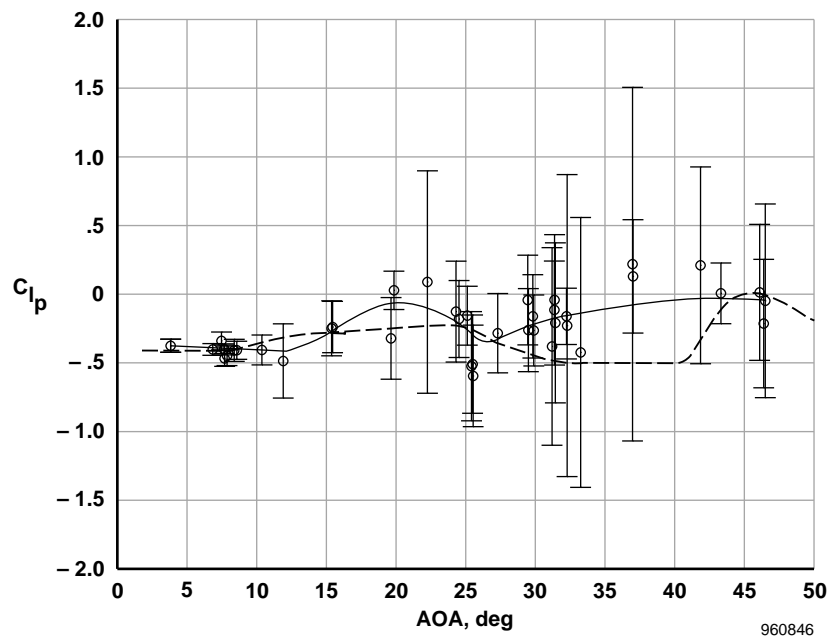
(b) $C_{n_{\delta_r}}$ as a function of AOA.

Figure 10. Rudder derivatives as functions of AOA.



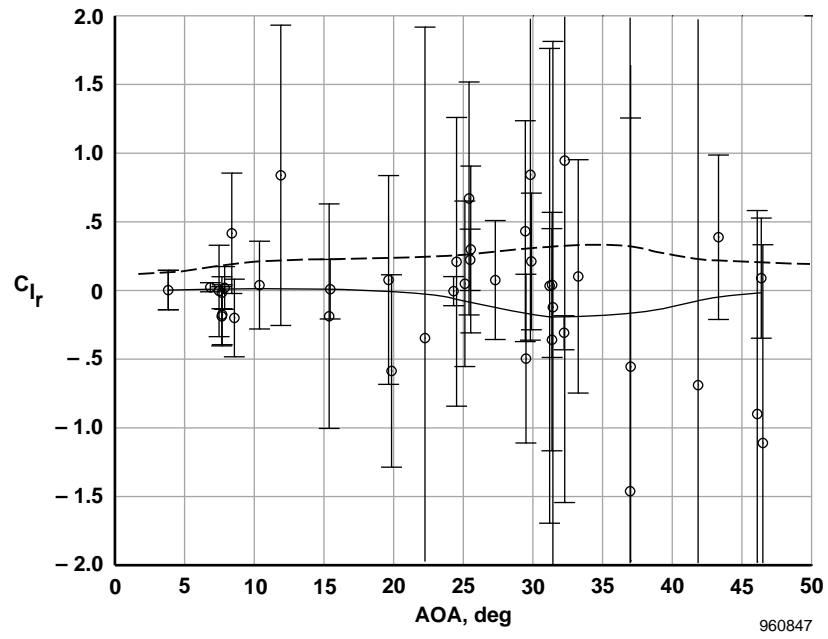
(c) $C_{Y_{\delta_r}}$ as a function of AOA.

Figure 10. Concluded.

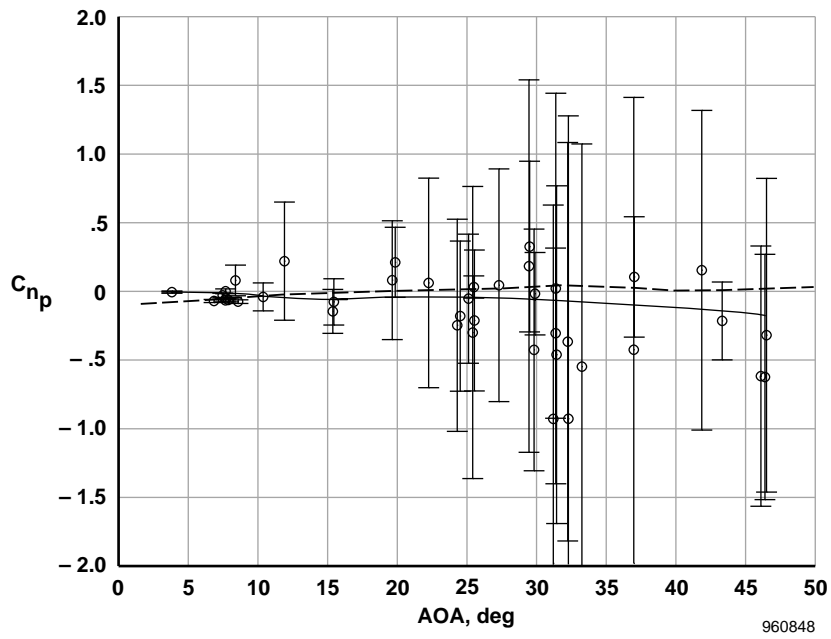


(a) C_{l_p} as a function of AOA.

Figure 11. Rotary derivations as functions of AOA.

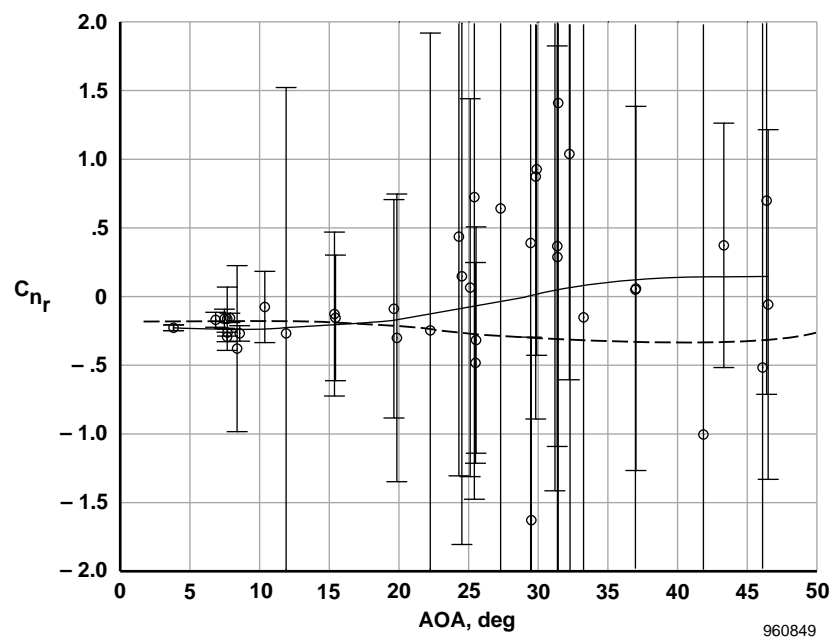


(b) C_{l_r} as a function of AOA.



(c) C_{n_p} as a function of AOA.

Figure 11. Continued.



(d) C_{n_r} as a function of AOA.

Figure 11. Concluded.

REPORT DOCUMENTATION PAGE			Form Approved OMB No. 0704-0188	
<small>Public reporting burden for this collection of information is estimated to average 1 hour per response, including the time for reviewing instructions, searching existing data sources, gathering and maintaining the data needed, and completing and reviewing the collection of information. Send comments regarding this burden estimate or any other aspect of this collection of information, including suggestions for reducing this burden, to Washington Headquarters Services, Directorate for Information Operations and Reports, 1215 Jefferson Davis Highway, Suite 1204, Arlington, VA 22202-4302, and to the Office of Management and Budget, Paperwork Reduction Project (0704-0188), Washington, DC 20503.</small>				
1. AGENCY USE ONLY (Leave blank)		2. REPORT DATE February 1997		3. REPORT TYPE AND DATES COVERED Technical Memorandum
4. TITLE AND SUBTITLE Extraction of Lateral-Directional Stability and Control Derivatives for the Basic F-18 Aircraft at High Angles of Attack			5. FUNDING NUMBERS WU505-68-50	
6. AUTHOR(S) Kenneth W. Iliff and Kon-Sheng Charles Wang				
7. PERFORMING ORGANIZATION NAME(S) AND ADDRESS(ES) NASA Dryden Flight Research Center P.O. Box 273 Edwards, California 93523-0273			8. PERFORMING ORGANIZATION REPORT NUMBER H-2143	
9. SPONSORING/MONITORING AGENCY NAME(S) AND ADDRESS(ES) National Aeronautics and Space Administration Washington, DC 20546-0001			10. SPONSORING/MONITORING AGENCY REPORT NUMBER NASA TM-4786	
11. SUPPLEMENTARY NOTES				
12a. DISTRIBUTION/AVAILABILITY STATEMENT Unclassified—Unlimited Subject Category 08			12b. DISTRIBUTION CODE	
13. ABSTRACT (Maximum 200 words) <p>The results of parameter identification to determine the lateral-directional stability and control derivatives of an F-18 research aircraft in its basic hardware and software configuration are presented. The derivatives are estimated from dynamic flight data using a specialized identification program developed at NASA Dryden Flight Research Center. The formulation uses the linearized aircraft equations of motions in their continuous/discrete form and a maximum likelihood estimator that accounts for both state and measurement noise. State noise is used to model the uncommanded forcing function caused by unsteady aerodynamics, such as separated and vortical flows, over the aircraft. The derivatives are plotted as functions of angle of attack between 3° and 47° and compared with wind-tunnel predictions. The quality of the derivative estimates obtained by parameter identification is somewhat degraded because the maneuvers were flown with the aircraft's control augmentation system engaged, which introduced relatively high correlations between the control variables and response variables as a result of control motions from the feedback control system.</p>				
14. SUBJECT TERMS Aerodynamics, Flight-to-wind-tunnel comparisons, F-18 aircraft, High angle of attack, Maximum likelihood estimation, Parameter identification, Stability and control derivatives			15. NUMBER OF PAGES 40	
			16. PRICE CODE A03	
17. SECURITY CLASSIFICATION OF REPORT Unclassified	18. SECURITY CLASSIFICATION OF THIS PAGE Unclassified	19. SECURITY CLASSIFICATION OF ABSTRACT Unclassified	20. LIMITATION OF ABSTRACT Unlimited	